

Time-Dependent Propagation of High Energy Laser Beams through the Atmosphere*

J. A. Fleck, Jr., J. R. Morris, and M. D. Feit

Lawrence Livermore Laboratory, University of California, Livermore, CA 94550, USA

Received 29 November 1975/Accepted 9 February 1976

Abstract. The computation of time-dependent three-space-dimensional laser beam propagation is described. The methods are applicable to the propagation of high energy laser beams through the atmosphere in the presence of a horizontal wind and turbulence for most situations of interest. Possible cases are propagation of cw beams through stagnation zones, multi-pulse propagation, including the self-consistent treatment of pulse self-blooming, and propagation involving transonic slewing. The solution of the Maxwell wave equation in Fresnel approximation is obtained by means of a discrete Fourier transform method, which, surprisingly, gives excellent results for diffraction problems. The latter provide a stringent test for the accuracy of any solution method. Considerable use is also made of discrete Fourier transform methods in solving the hydrodynamic equations. The treatment of turbulence is based on the generation of random phase screens at each calculation step along the propagation path. In a time-dependent calculation the random phase screens can be either made to move with the wind at a given propagation position or generated anew for each successive time.

PACS Code: 42.10

The thermal blooming of intense laser beams in the atmosphere is well understood for steady-state conditions and wind velocities substantially below sound speed [1, 2]. There is also reasonably good understanding of the time-dependent blooming of single short axially symmetric pulses [3–5]. There remain, however, a number of categories of high-energy-propagation problems for which understanding is either incomplete or only beginning. Among these are the following:

- Propagation in the presence of transonic and supersonic winds brought about by beam slewing.
- Propagation through “dead” or stagnation zones, where the wind velocity goes to zero.
- Propagation of multi-pulse trains.

* This work was done under contract to the Advanced Research Projects Agency of the Department of Defense, the Army Missile Command, Huntsville, Alabama, and the U.S. Energy Research and Development Administration.

The solution of propagation problems in the above-mentioned categories requires either a more general treatment of steady-state hydrodynamics than has hitherto been used, or a time-dependent—sometimes referred to as a “four-dimensional”—approach to the solution of the propagation problem as a whole. The time-dependent treatment is absolutely essential for treating problems in the second category.

This paper describes the contents of a general “four-dimensional” computer code (hereafter referred to as “Four-D” code,) and provides specific numerical examples of its use. The Four-D code is capable of treating problems in the three categories listed above and of modeling the effect of atmospheric turbulence on propagation by the method of random phase screens [6, 7].

For steady-state blooming and wind velocities substantially below sound speed the simple steady-state isobaric (infinite sound speed) approximation to

the linearized hydrodynamic equations is accurate, and one can integrate across the heat source in the direction of the wind to obtain the density changes that affect the propagation of the laser beam [1–3]. The same isobaric approximation applies even for time-dependent density changes such as occur when a cw beam crosses a stagnation zone, although obtaining an accurate integration of the convective equation governing the density changes is more complicated.

When beam slewing creates effective wind velocities of the order of the sound speed, the simple isobaric approximation is no longer valid, and a solution of the complete system of hydrodynamic equations is required. Wherever the wind velocity exactly equals the ambient or unheated medium sound speed, the linearized hydrodynamic equations possess no steady state solution and density changes can, in principle, increase without limit. This behavior is, of course, precluded by the nonlinear properties of the flow.

Detailed numerical solutions [8] of the nonlinear hydrodynamic equations indicate the following behavior for transonic winds. For wind velocities up to and slightly above ambient sound speed, i.e. for $M_0 \sim 1$, a weak shock wave develops and propagates upwind creating an increase in the heated medium sound speed; this increase in sound speed is such as to make the Mach number M of the wind speed relative to the sound speed in the heated medium always less than 1. If the wind speed is further increased above ambient sound speed, the shock disappears and the heated-medium sound speed returns to the ambient medium value. Now, however, M ends up being greater than 1. Since density changes are always small, the linearized hydrodynamic equations govern the steady state solution throughout. In order to apply them it would only be necessary to know the correct value of M , since it is M and not M_0 that determines the steady-state-density properties. We know that $M \neq 1$ and that, except for wind velocities very close to $M_0 = 1$, $M = M_0$ is a good approximation. This suggests that we can get a good estimate of thermal blooming under conditions of transonic slewing by applying steady-state linearized hydrodynamic solutions all along the propagation path, avoiding only the z position for which $M_0 = 1$, but including z -positions for which M_0 is very close to 1. Bradley [9] has shown that even if the singular point with $M_0 = 1$ is included in the path, overall phase changes are minimal due to the weakness of the singularity. This conclusion is also borne out in the

detailed calculations of transonic slewing to be described in this paper.

In the description of the propagation of multi-pulse beams the time-dependent isobaric approximation is adequate for describing the influence of a given pulse on subsequent pulses in the train. But a more accurate treatment of the acoustic equations is required in order to account for the pulses self-blooming effect. In the code described here this is done by assuming a triangular pulse shape in time and evaluating the exact density change for the time of the triangle's apex by a two-dimensional Fourier transform. Comparing single-pulse propagation based on such a calculation of the density with a solution obtained using a pulse blooming code enabling many sampling times in the pulse has shown this triangular approximation to be a good one for moderate self-blooming. It is clearly possible to allow many sampling times within a given pulse for the self-blooming calculation, although it would add greatly to the complexity of the multipulse problem.

Ideally, one would like to deal with all propagation phenomena, whether time-dependent or time-independent, in terms of the most general treatment of the hydrodynamic equations within the framework of a single code. As a practical matter the construction of such a code has required the definition of a number of special flow regimes with different treatments of the hydrodynamics in each.

For example, a time-dependent generalization of the isobaric flow approximation suffices for treating the hydrodynamics encountered in dead-zone problems. But, on the other hand, a more accurate solution of the hydrodynamic equations is required in dealing with steady-state blooming involving a sonic point along the propagation path. In particular, the linearized steady-state hydrodynamic equations are elliptic if $M < 1$, requiring a Fourier transform method of solution; whereas they are hyperbolic for $M > 1$, requiring a solution by the method of characteristics.

The time-dependent structure of the code makes it a convenient tool for studying long-time averages of the effect of turbulence on beam propagation. One may choose between options of allowing a single random phase screen to move with the wind in time or of choosing a different random phase screen for each sampling time in the pulse. At the end of the pulse time history a time-averaged fluence is calculated for each z -station specified for editing.

The general features of the Four-D propagation code are outlined in Table 1 and described in detail in

Table 1. Basic outline of Four-D propagation code

Variables	$x, y, z, t,$ where x, y are transverse coordinates and z is axial displacement.
Form of propagation equation	Scalar wave equation in parabolic approximation $2ik \frac{\partial \mathcal{E}}{\partial z} = \nabla_{\perp}^2 \mathcal{E} + k^2(n^2 - 1)\mathcal{E}$
Method of solving propagation equation	Symmetrized split operator, finite Fourier series, fast Fourier transform (FFT) algorithm $\mathcal{E}^{n+1} = e^{-\frac{iA_z}{4k}\nabla_{\perp}^2} e^{-\frac{iA_z}{2k}} e^{-\frac{iA_z}{4k}\nabla_{\perp}^2} \mathcal{E}^n$ $\chi = k^2(n^2 - 1),$
Hydrodynamics for steady-state problems	Uses exact solution to linear hydrodynamic equations. Fourier method for $M < 1$. Characteristic method for $M > 1$. Solves $v \frac{\partial \varrho_1}{\partial x} + \varrho_0 \nabla_{\perp} \cdot \mathbf{v}_1 = 0$ $\varrho_0 v \frac{\partial \mathbf{v}_1}{\partial x} + \nabla_{\perp} p_1 = 0$ $v \frac{\partial}{\partial x}(p_1 - c_s^2 \varrho_1) = (\gamma - 1)\alpha I$
Transonic slewing	Steady-state calculation valid for all Mach numbers except $M = 1$.
Treatment of stagnation zone problems	Code can be used arbitrarily close to $M = 1$ Time-dependent isobaric approximation. Transient succession of steady-state density changes, i.e. solves $\frac{\partial \varrho_1}{\partial t} + v \frac{\partial \varrho_1}{\partial x} = - \left(\frac{\gamma - 1}{c_s^2} \right) \alpha I$
Treatment of multipulse density changes and blooming	Density changes resulting from previous pulses in train calculated with isobaric approximation. Density changes resulting from the same pulse calculated using acoustic equations and assumption of triangular pulse shape. Takes two-dimensional Fourier transform of
Method of calculating density change for individual pulse in train	$-\frac{\alpha \tilde{I} t_p}{c_s^2} \left\{ 1 - \frac{\sin^2 \left[\frac{1}{2} c_s (k_x^2 + k_y^2)^{1/2} t_p \right]}{\left[\frac{1}{2} c_s (k_x^2 + k_y^2)^{1/2} t_p \right]^2} \right\}$
Treatment of turbulence	where \tilde{I} is Fourier transform of intensity, and t_p is the time-duration of each pulse Uses phase-screen realization of Bradley and Brown with von Karman spectrum. Phase screens can be selected either to be independent of time or to move with the wind.
Treatment of lens optics	Uses $\frac{1}{z_f} = \frac{1}{z_T} + \frac{1}{z_L}$ where z_f is the desired lens focal length, z_T is the lens focal length that is compensated for by a lens transformation, and z_L is the lens focal length used explicitly in calculation.
Code output	Isointensity, isodensity, isophase and spectrum contours. Intensity averaged over contours. Plots of intensity, phase, density, spatial spectrum along specific directions, etc. at specific times. Plots of peak intensity and average intensity vs time. Spatial mesh, 64×64 , 35 sampling times, no restriction on number of axial space increments.
Numerical capacity when used with CDC 7600 and restricted to internal memory (large and small core)	Number of space increments in x and y directions must be equal and expressible as a power of 2. Propagation path can be broken up into segments each having separate data. In particular A_z step can be different for each segment.
Problem zoning features	The running time will vary with edit frequency and other problem conditions. However, a reasonable average is 0.9 s per z -step per time step for a 64×64 mesh.
Problem running time on CDC 7600 computer	

Table 2. Basic outline of axially symmetric pulse propagation code

Variables	r, z, t
Method of solving propagation equations	Utilizes cubic spline representation of field in radial direction and implicit differencing in z -direction. Implicit field equations solved by backsubstitution algorithm.
Treatment of hydrodynamics	Fully nonlinear equations treated by implicit continuous Eulerian (ICE) method in r, t space
Treatment of differencing in time	Independent time-step increments for hydrodynamic and propagation portions of calculation. Hydrodynamic time step based on incremental changes in hydrodynamic variables.
Maximum problem size	Four hundred radial points, 31 sampling time intervals in propagation calculation.

the body of the paper. The code has been organized as a collection of a reasonably large number of subroutines, with the appropriate hydrodynamic subroutine being determined by the nature of the problem.

In order to test the triangular pulse approximation used in computing multi-pulse density changes, a single-pulse time-dependent axially symmetric thermal blooming code was developed. This code was created by modifying a propagation code designed to model laser breakdown of gases in cylindrically symmetric geometry and has the unique feature of possessing a complete nonlinear hydrodynamics calculation [10, 11]. The general features of this code are outlined in Table 2.

1. Treatment of the Propagation Equation

Maxwell's wave equation in the parabolic or Fresnel approximation is

$$2ik \left(\frac{n \partial \mathcal{E}}{c \partial t} + \frac{\partial \mathcal{E}}{\partial z} \right) = V_{\perp}^2 \mathcal{E} + k^2(n^2 - 1)\mathcal{E}, \quad (1)$$

where n is the refractive index, \mathcal{E} is a slowly varying field amplitude and the intensity I is given in terms of \mathcal{E} by $I = |\mathcal{E}|^2 \exp(-\alpha z)$, where α is the absorption coefficient. Also $k = 2\pi/\lambda$, $V_{\perp}^2 = \partial^2/\partial x^2 + \partial^2/\partial y^2$, and $n^2 - 1 = \delta\varepsilon$ is the hydrodynamically induced change in permittivity. It is most convenient to work in terms of a retarded time $t' = t - nz/c$. Rewriting (1) in terms of t' gives

$$2ik \frac{\partial \mathcal{E}}{\partial z} = V_{\perp}^2 \mathcal{E} + k^2 \delta\varepsilon \mathcal{E}, \quad (2)$$

where $\mathcal{E} = \mathcal{E}(x, y, z, t')$. Hereafter the prime on t' will be dropped, and it will be understood that t is always measured with reference to the time of arrival of the front of the pulse at the position z in question.

Let $\mathcal{E}^n(x, y)$ be the complete solution to (2) at $z=z^n$. Then the solution at $z^{n+1}=z^n+\Delta z$ may be written formally in terms of \mathcal{E}^n as

$$\mathcal{E}^{n+1} = \exp \left[-\frac{i}{2k} \left(\Delta z V_{\perp}^2 + k^2 \int_{z^n}^{z^{n+1}} \delta\varepsilon dz \right) \right] \mathcal{E}^n. \quad (3)$$

In general the operators V_{\perp}^2 and $\delta\varepsilon$ do not commute. It is shown in Appendix A, however, that for any analytic function $\delta\varepsilon$, i.e. one that can be represented as a Taylor series in z , the solution (3) can be replaced with a second-order accuracy by one involving the symmetrized split operator [12] form

$$\mathcal{E}^{n+1} = e^{-\frac{i}{4k} \Delta z V_{\perp}^2} e^{-\frac{ik}{2} \Delta z \bar{\delta\varepsilon}} e^{-\frac{i}{4k} \Delta z V_{\perp}^2} \mathcal{E}^n, \quad (4)$$

where $\bar{\delta\varepsilon}$ is understood to mean

$$\bar{\delta\varepsilon} = \frac{1}{\Delta z} \int_{z^n}^{z^{n+1}} \delta\varepsilon dz. \quad (5)$$

The symmetrization exhibited in (4) is actually more important in form than in substance, since after the first upgrading of the phase the half steps of propagation can be combined into single propagation steps according to the rule

$$e^{-\frac{i}{4k} \Delta z V_{\perp}^2} e^{-\frac{i}{4k} \Delta z V_{\perp}^2} = e^{-\frac{i}{2k} \Delta z V_{\perp}^2}. \quad (6)$$

The algorithm for propagating the field over a distance Δz thus consists of an incrementing of the phase in accordance with nonlinear medium changes, followed by a vacuum propagation of the resulting field over a distance Δz , i.e. solving the equation

$$2ik \frac{\partial \mathcal{E}}{\partial z} = V_{\perp}^2 \mathcal{E}. \quad (7)$$

In order to introduce the symmetrization it is only necessary to initiate the procedure by a step of vacuum propagation from $z=0$ to $z=\Delta z/2$.

With the solution expressed in the factored form (4) it is easy to see that, to second order, focused beam coordinate transformations can be applied without regard to the nonlinear term in (2) and thus need only be applied to the vacuum propagation (7). One of the simplest such transformations is one originally due to Talanov [13]. Let the field be represented at $z=0$ by

$$\mathcal{E}(r, 0) = e^{ik(x^2 + y^2)/2z_f} \mathcal{E}'(r, 0), \quad (8)$$

where the phase front $k(x^2 + y^2)/2z_f$ is the result of passing a beam through a thin spherical lens with focal length z_f . Then it can be shown (see Appendix B) that the field at $z=\Delta z$ can be represented by

$$\begin{aligned} \mathcal{E}(r, \Delta z) &= \left(\frac{1}{1 - \frac{\Delta z}{z_f}} \right) \\ &\cdot \mathcal{E}' \left(\frac{r_\perp}{1 - \frac{\Delta z}{z_f}}, \frac{\Delta z}{1 - \frac{\Delta z}{z_f}} \right) e^{\frac{ikr^2}{2z_f(1 - \Delta z/z_f)}}, \end{aligned} \quad (9)$$

where $r=x^2+y^2$. In order to apply the formula (9) it is necessary to solve the free propagation equation (7) out to the adjusted distance

$$\Delta z' = \frac{\Delta z}{1 - \frac{\Delta z}{z_f}} \quad (10)$$

with $\mathcal{E}'(r, 0)$ as an initial condition. After this is done, both the field amplitude and the mesh are rescaled according to a geometric optics transformation, which consists of multiplying all of the $\mathcal{E}'(r_\perp, \Delta z')$ values in computing storage by the factor $1/(1 - \Delta z/z_f)$ and then changing the names of the corresponding x and y coordinates to x' and y' according to the rule

$$\begin{aligned} x' &= (1 - \Delta z/z_f) x \\ y' &= (1 - \Delta z/z_f) y. \end{aligned} \quad (11)$$

Thus the dimensions of the describing mesh are either shrunken or dilated according to whether the focal length z_f is positive or negative. (Note that total beam power is conserved by this rescaling.) At the end of the step the correct phase of \mathcal{E} is derived by adding to the phase of \mathcal{E}' the expression

$$\frac{kr^2}{2(z_f - \Delta z)}, \quad (12)$$

which represents the phase front imposed by a spherical lens focused at a distance $z_f - \Delta z$. For the next propagation step one may either propagate the field including the explicit phase contribution (12) on the existing mesh without further use of the lens transformation, or one may compensate for the phase (12) with the lens transformation (9) using the new focal distance $z'_f = z_f - \Delta z$.

In general, one will not wish to compensate for the full phase contribution of a given lens with the transformation (9). This is because (9) causes the grid to transform in accordance with geometric optics and eventually either diffraction or thermal blooming will cause the beam to expand relative to the resulting mesh enough to collide with the boundaries, aborting the problem. Instead one should impose explicitly a phase front $k(x^2 + y^2)/2z'_f$, associated with some focal length z'_f , on the initial beam and compensate for an additional phase front associated with a focal length z''_f using a lens transformation, where z'_f and z''_f are related to the true focal length z_f by

$$\frac{1}{z_f} = \frac{1}{z'_f} + \frac{1}{z''_f}. \quad (13)$$

For strong blooming one will wish to keep the beam inside the grid by taking z'_f as small as possible. Obviously the minimum useable value of z'_f will be determined by the requirement that the complex exponential in (8) should be accurately represented on the calculational mesh. An excessively small choice of z'_f can show up as a strong modulation of the spectral power density of E due to an aliasing in the calculated values of $\exp(ikr^2/2z'_f)$. The lens transformation embodied in (9) and (13) has the advantage of simplicity and has been successfully applied to a variety of problems. Other transformations of similar intent but of different form are in use in a variety of other codes [1, 2]. The more general transformation outlined in the appendix allows for two focal lengths and can be used to compensate for astigmatic effects of thermal blooming.

The numerical solution of (7) is based on the representation of $\mathcal{E}(x, y, z)$ as a finite two-dimensional Fourier series [14]

$$\mathcal{E}(x, y, z) = \sum_{m=-\frac{N}{2}+1}^{\frac{N}{2}} \sum_{n=-\frac{N}{2}+1}^{\frac{N}{2}} \mathcal{E}_{mn}(z) e^{\frac{2\pi i(mx + ny)}{N}}$$

which exhibits periodicity on a square of side $L = N\Delta z = N\Delta y$ in $x-y$ space. On substituting expression

(14) into (7), the following exact expression for $\mathcal{E}_{mn}(\Delta z)$ is obtained

$$\mathcal{E}_{mn}(\Delta z) = \mathcal{E}_{mn}(0) e^{\frac{i}{2k} \left(\frac{2\pi}{N} \right)^2 (m^2 + n^2) \Delta z}. \quad (15)$$

The initial values $\mathcal{E}_{mn}(0)$ are evaluated numerically by an application of the two-dimensional discrete Fourier transform (DFT) [15]

$$\mathcal{E}_{mn}^D = \sum_{j=0}^{N-1} \sum_{k=0}^{N-1} \mathcal{E}(j, k) e^{-\frac{2\pi i(mj+nk)}{N}}, \quad (16)$$

where $\mathcal{E}(j, k) = \mathcal{E}(j\Delta x, k\Delta y, 0)$. The two-dimensional DFT is in turn executed as a sequence of $2N$ one-dimensional DFT operations defined by

$$\mathcal{E}_m^D = \sum_{j=0}^{N-1} \mathcal{E}(j) e^{-\frac{2\pi imj}{N}}, \quad (17)$$

where the $\mathcal{E}(j)$ represent sampled values taken along the appropriate (x or y) direction. The numerical evaluation of (17) is done with the fast Fourier transform (FFT) algorithm [14]. To obtain the sampled field values $\mathcal{E}(j\Delta x, k\Delta y, z)$ from (14), it is necessary to evaluate a sequence of $2N$ inverse DFT operations of the form

$$\mathcal{E}(j) = \frac{1}{N} \sum_{m=0}^{N-1} \mathcal{E}_m^D e^{\frac{2\pi imj}{N}}. \quad (18)$$

At this juncture it is important to review the criteria for the accuracy of a representation of a function as a finite Fourier series such as in (14). Let $\mathcal{E}(x)$ be a function whose spectrum $\mathcal{E}(k)$ vanishes for $|k| \geq k_{\max} = (N/2)(2\pi/L)$, and let $\mathcal{E}(x)$ also vanish outside the interval $0 \leq x \leq L$. Then $\mathcal{E}(x)$ is represented exactly by the Fourier series

$$\mathcal{E}(x) = \sum_{m=-N/2}^{N/2} \mathcal{E}_m e^{\frac{2\pi i mx}{L}}, \quad (19)$$

and the Fourier coefficients \mathcal{E}_m can be represented exactly in terms of the sampled function values

$\mathcal{E}(j\Delta x) = \mathcal{E}_j$ by means of the DFT relations

$$\begin{aligned} \mathcal{E}_m &= \frac{1}{L} \sum_{j=0}^{N-1} \mathcal{E}_j e^{\frac{-2\pi ij m}{N}}, \quad 0 \leq m \leq \frac{N}{2} \\ \mathcal{E}_m &= \frac{1}{L} \sum_{j=0}^{N-1} \mathcal{E}_j e^{\frac{-2\pi ij(N-m)}{N}}, \quad -\frac{N}{2} < m < 0 \\ \mathcal{E}_{-N/2} &= \mathcal{E}_{N/2}. \end{aligned} \quad (20)$$

This implies that a solution of (7) and consequently the application of the propagation operators in (4) is for all practical purposes exact so long as $\mathcal{E}(x, y)$

and \mathcal{E}_{mn} are negligible near the boundaries of their respective meshes in the $x-y$ and k_x-k_y space, respectively. Under these circumstances the only errors involved in the application of (3) are commutation errors and errors associated with updating $\delta\mathcal{E}(x, y)$ a finite number of times.

A periodic monitoring of $|\mathcal{E}(x, y)|^2$ and $|\mathcal{E}_{mn}|^2$ during the propagation calculation can be used to establish the accuracy of the free propagation portion of the calculation. As soon as the solution has been detected graphically to have collided with the boundary in configuration space or k -space, the solution is no longer trustworthy. If the solution has not collided, complicated intensity or spectral patterns are believable at the sampled points in the appropriate space.

The opinion has been widely expressed that a straightforward application of DFT methods will give inaccurate or unacceptable results whenever the problem to which they are applied involves discontinuities, since the latter tend to involve broad spectra and the possibility of Gibbs phenomena. This conjecture is certainly not true in general as we shall see in examining a diffraction problem in this section and a flow problem in Section 5.

One of the most stringent tests of a propagation method is its ability to predict diffraction patterns. The DFT method gives excellent results for a minimal number of mesh points.

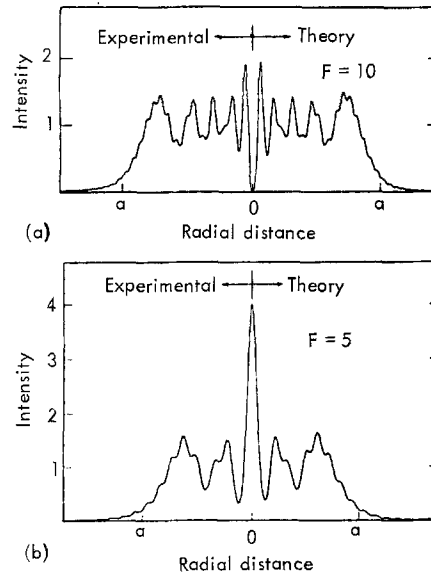


Fig. 1. Experimental and theoretical diffraction patterns (a) Fresnel number of 10. (b) Fresnel number of 5. Theoretical curves calculated from finite difference method using grid of 1800 points

Figures 1a and 1b are reproductions of diffraction patterns for a uniformly illuminated circular aperture obtained by theoretical calculation and experimental measurements by Campillo et al [16]. The theoretical results shown in Figure 1 were obtained by solving (7) numerically in cylindrical coordinates using a finite-difference scheme and a uniform grid of 1800 radial increments with a total of 400 increments under the aperture [17].

Figures 2–7 show the results of solving (7) by the DFT method. Specifically, a DFT cosine transform

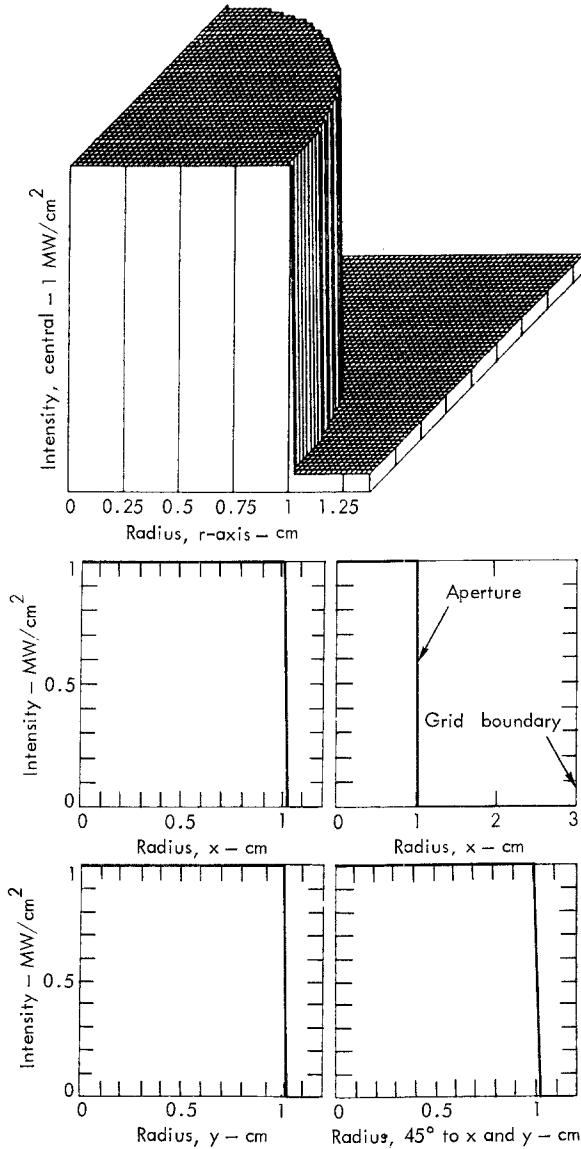


Fig. 2. Initial conditions for uniformly illuminated aperture used in two-dimensional DFT calculation. Grid size is 128×128 . There are 43 grid points under the aperture. Second two-dimensional plot shows size of grid relative to aperture

was used on a 128×128 grid. Figures 2–4 show the results of using a “hard” aperture, or requiring that $\mathcal{E} = 0$ for $x^2 + y^2 \geq a^2 = 1.0$ at $z=0$. This initial condition leads to the flat intensity distribution with a slightly scalloped boundary shown in Figure 2. The computational grid spacing is such that there are 43 equal space increments along either the x or y axis inside the aperture. The dotted curves plotted in Figures 3, 4, 6, and 7 represent the results of digitizing the experimental curves in Figure 1. The agreement between the calculated and experimental pattern at the mesh points for the hard aperture is very good for a Fresnel number $N = 10$, and it is excellent for $N = 5$.

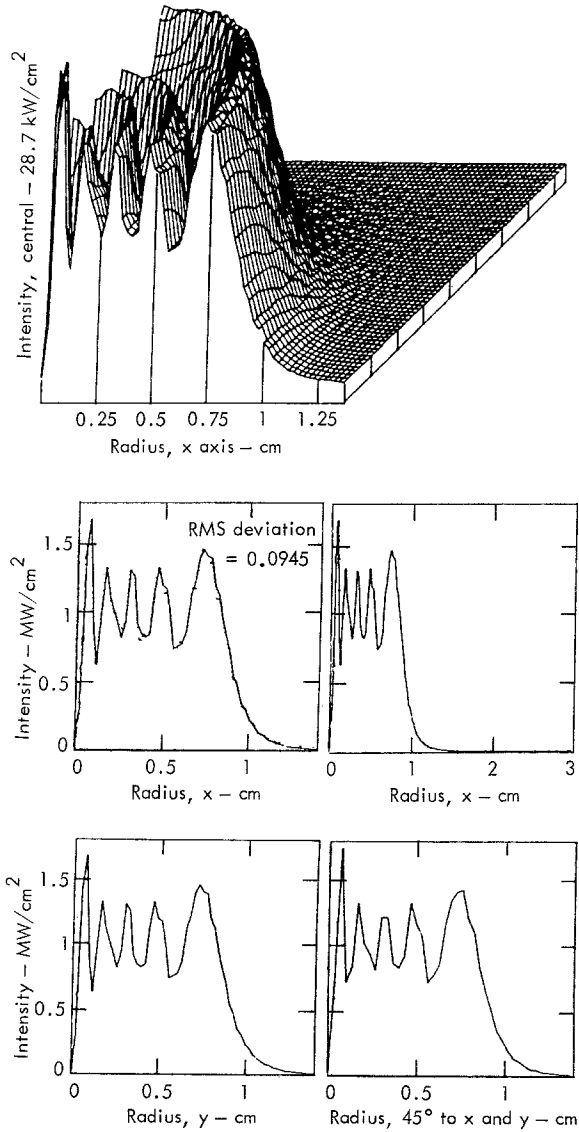


Fig. 3. Results for DFT calculation Fresnel number 10. Solid line is calculation, points are digitized experimental data

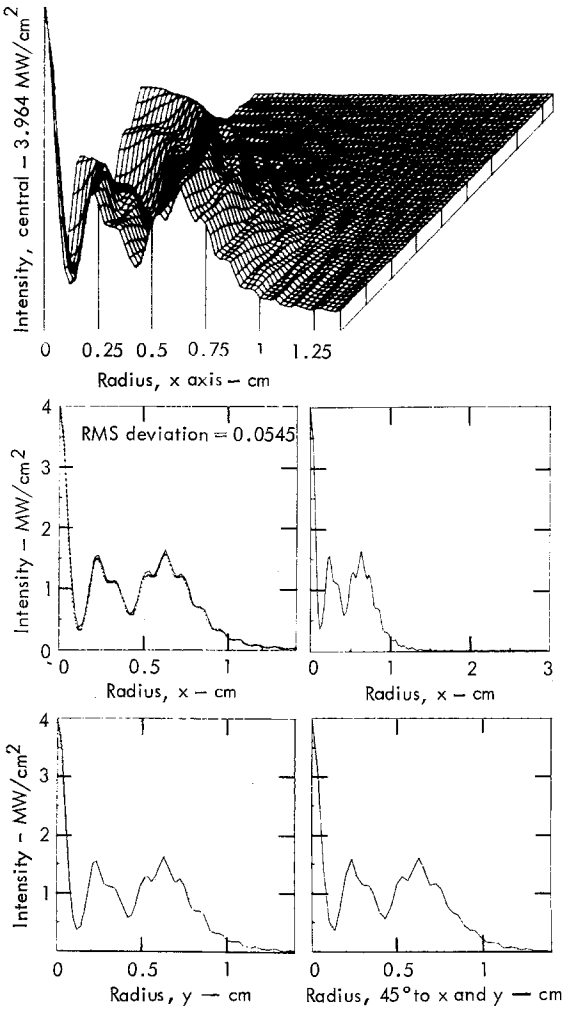


Fig. 4. Same as Figure 3 for Fresnel number of 5

Figures 5–7 show the results of performing the calculation using as a field distribution at $z=0$ the “super” Gaussian distribution

$$E = \exp \left[-\left(\frac{r}{a} \right)^{143} \right], \quad (21)$$

which has the effect of apodizing or “softening” the aperture slightly (Fig. 5). The agreement between calculation and experiment as measured by rms deviation is actually poorer for the apodized aperture at both $N=10$ and $N=5$ than it is for the hard aperture although apodizing does improve the circular symmetry of the diffraction pattern at $N=10$. Lowering the value of the exponent in (21) does not improve matters, since it has the effect of altering the diffraction pattern. Even a reduction of the exponent to a

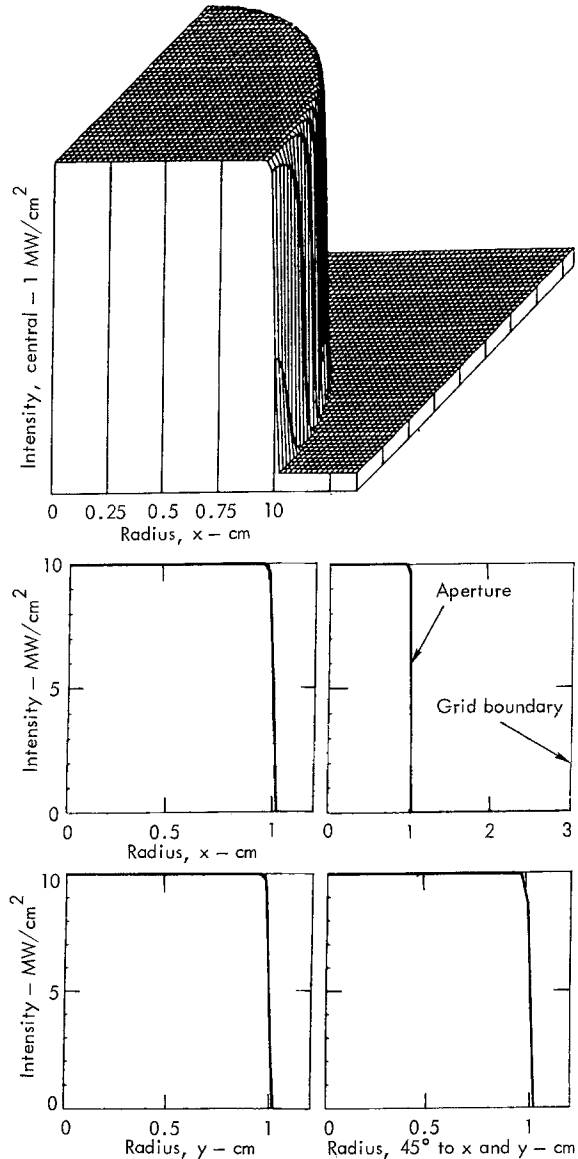


Fig. 5. Initial conditions for super-Gaussian initial field distribution

value of 100 already produces significant deviations from the experimental pattern.

The implications of these results are that apodizing apertures in the calculation of linear diffraction effects should be used very sparingly, but the use of hard apertures with the DFT method introduces no difficulties whatever and in fact leads to very accurate results. When nonlinear effects are present in the propagation problem, on the other hand, the possibility of aliasing is always present (see discussion in Section 4) and a small amount of apodizing may be beneficial.

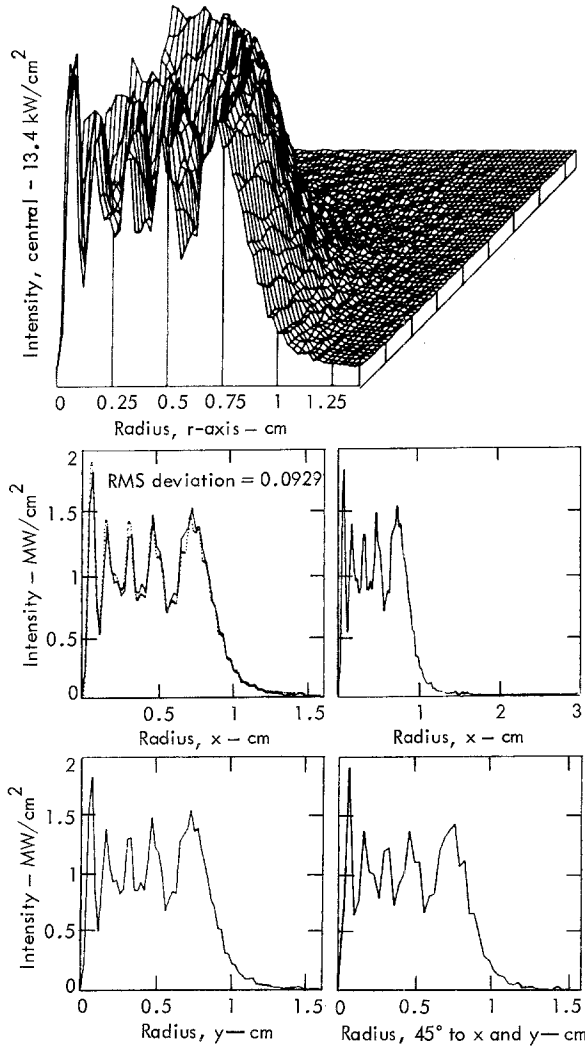


Fig. 6. Comparison with experiment for super-Gaussian, Fresnel number 10

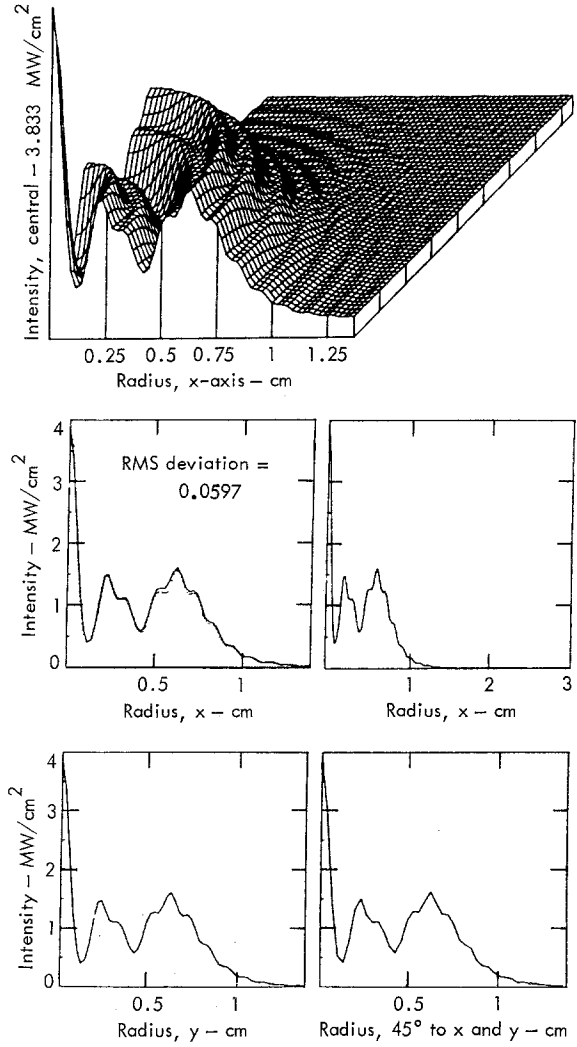


Fig. 7. Comparison with experiment for Fresnel number 5, super Gaussian initial shape

2. Treatment of Steady-State Hydrodynamics and Density Variations

Treatments of the steady-state hydrodynamic motion of air resulting from laser heating have hitherto been based on the isobaric assumption [1, 2] and are valid only for wind velocities well below sound speed. In this section we outline a numerical treatment of the steady-state linearized hydrodynamic equations, which are valid for all wind speed Mach numbers except $M=1$. In that case, as is well known, no steady-state solution to the linearized equation exists.

The linearized hydrodynamic equations in the presence of a wind can be written

$$\frac{d\varrho_1}{dt} + \varrho_0 \nabla \cdot \mathbf{v}_1 = 0 \quad (22a)$$

$$\varrho_0 \frac{dv_1}{dt} = -\nabla p_1 \quad (22b)$$

$$\frac{d}{dt}(p_1 - c_s^2 \varrho_1) = (\gamma - 1) \alpha I. \quad (22c)$$

In the above equations d/dt represents a substantial derivative, in the direction of the wind, which has

a velocity v

$$\frac{d}{dt} = \frac{\partial}{\partial t} + v \frac{\partial}{\partial x}. \quad (23)$$

Here ϱ_1 , p_1 and v_1 are perturbations in density, pressure, and velocity, and c_s is the sound speed, defined by

$$c_s^2 = \frac{\gamma \varrho_0}{p_0}, \quad (24)$$

where ϱ_0 and p_0 are the density and pressure for the undisturbed atmosphere and γ is the specific heat ratio.

In the isobaric or infinite sound speed approximation p_1 is neglected in (22c). This results in the following equation for ϱ_1

$$\frac{\partial \varrho_1}{\partial t} + v \frac{\partial \varrho_1}{\partial x} = - \frac{(\gamma - 1)}{c_s^2} \alpha I. \quad (25)$$

Equation (25) describes a time-dependent succession of steady-state density changes and is accurate provided that wind speeds are small in comparison with c_s and density changes occur on a time scale long in comparison with a sonic transit time across the beam. Equation (25) can be used for describing density changes in stagnation zones, provided that insufficient time has elapsed to let buoyancy effects become important. It will be shown, however, that under practical conditions beam deterioration due to the presence of a dead zone occurs on such a short time scale as to prevent buoyancy effects from becoming important.

The establishment of a steady-state density distribution will occur in a time of the order of $a/|v - c_s|$, where a is the beam radius, except possibly at positions where v lies extremely close to the sound speed. Even for those positions, a bounded steady-state solution is always guaranteed by the nonlinear behavior of the hydrodynamic equations which changes the sound speed in such a way as to keep M in the disturbed medium different from 1.

If p_1 and v_1 are eliminated from (22), one obtains the following equation for ϱ_1

$$\left[\frac{d^2}{dt^2} - c_s^2 V^2 \right] \frac{d\varrho_1}{dt} = (\gamma - 1) \alpha V^2 I. \quad (26)$$

For a steady state, (26) becomes

$$\left[\frac{\partial^2}{\partial y^2} + (1 - M^2) \frac{\partial^2}{\partial x^2} \right] \frac{\partial \varrho_1}{\partial x} = - \frac{(\gamma - 1)}{c_s^2 v} \alpha V^2 I. \quad (27)$$

In developing a numerical procedure for solving (27) it is necessary to take into account the fact that this equation is elliptic for $M < 1$ and hyperbolic for $M > 1$. Thus a completely different approach is required for subsonic and supersonic situations. For $M < 1$ a Fourier method is the obvious choice, and we write

$$\phi(x, y) = \frac{\partial \varrho_1}{\partial x} = \sum_m \sum_n \phi_{mn} e^{i(k_m x + k_n y)}, \quad (28)$$

where

$$k_m = \frac{2\pi m}{L}, \quad k_n = \frac{2\pi n}{L}. \quad (29)$$

Substituting expression (28) into (27) yields

$$\phi_{mn} = - [(\gamma - 1) \alpha / c_s^2 v] \frac{(k_m^2 + k_n^2) I_{mn}}{k_n^2 + (1 - M^2) k_m^2} \quad (30a)$$

$$= - [(\gamma - 1) \alpha / c_s^2 v] \frac{[m^2 + n^2]}{n^2 + (1 - M^2) m^2} I_{mn}, \quad (30b)$$

where I_{mn} is the appropriate Fourier coefficient of $I(x, y)$. Since there are no real roots in the denominator of (30a), it is possible to evaluate the sum (28) at the mesh points $(j\Delta x, l\Delta y)$ by applying a two-dimensional sequence of FFT operations, see (20). The final determination of $\varrho_1(x, y)$ is made by taking the two-dimensional inverse DFT of ϕ_{mn} and numerically evaluating the integral

$$\varrho_1(x, y) = \varrho_0(y) + \int_0^x \phi(x, y) dx. \quad (31)$$

The y -dependence of the “integration constant” $\varrho_0(y)$ is due to the presence of a source-dependent density disturbance at any finite distance upstream from the source. For a large enough upstream distance this y -dependence is probably unimportant. We shall therefore assume that $\varrho_0(y) = \text{const} = 0$. The exact value of this constant does not matter since only density differences are important in determining refractive properties. An additional fact that must be borne in mind in evaluating $\varrho_1(x, y)$ by means of (28) and (31) is that as M approaches 1, the influence of the source extends farther and farther in the y -direction. As a consequence of the periodic boundary conditions at $y=0$ and $y=L$, this will tend more and more to become a source of error. In order to minimize the effects of the unknown upstream density $\varrho_0(y)$ in (31) and the periodic boundary conditions at $y=0$ and $y=L$ we have extended the domain of integration

for the hydrodynamic calculation in both the x and y directions by an additional length L . The addition of the resulting buffer region has noticeably improved density solutions for $M \approx 0.9$.

For $M > 1$ the denominator of (30a) has real roots, which makes the Fourier method impractical to use since some way must be found to systematically isolate those terms in the sum with poles and express them in terms of line integrals. We turn instead to the method of characteristics which is applicable to a hyperbolic system. Taking the Fourier transform of (27) and solving for $\tilde{\varrho}_1(k_x, k_y)$ gives

$$\tilde{\varrho}_1(k_x, k_y) = \frac{[(\gamma - 1)\alpha/c_s^2 v](k_x^2 + k_y^2)}{ik_x[(M^2 - 1)k_x^2 - k_y^2]} \tilde{I}(k_x, k_y), \quad (32)$$

where \sim indicates the transform of the variable. The right-hand side of (32) can be decomposed into partial fractions giving

$$\begin{aligned} \tilde{\varrho}(k_x, k_y) = & [(\gamma - 1)\alpha/c_s^2 v] \tilde{I}(k_x, k_y) \\ & \cdot \left\{ -\frac{1}{ik_x} + \frac{M^2}{2(M^2 - 1)^{\frac{1}{2}}} \left[\frac{1}{(M^2 - 1)^{\frac{1}{2}} ik_x - ik_y} \right. \right. \\ & \left. \left. + \frac{1}{(M^2 - 1)^{\frac{1}{2}} ik_x + ik_y} \right] \right\}. \end{aligned} \quad (33)$$

It is evident from the form of the Fourier transform (33) that $\varrho(x, y)$ can be expressed as the sum of three contributions

$$\varrho_1 = \varrho_A + \varrho_B + \varrho_C \quad (34)$$

where ϱ_A , ϱ_B , and ϱ_C satisfy

$$\frac{\partial \varrho_A}{\partial x} = -\frac{(\gamma - 1)}{c_s^2 v} \alpha I \quad (35a)$$

$$\begin{aligned} (M^2 - 1)^{\frac{1}{2}} \frac{\partial \varrho_B}{\partial x} + \frac{\partial \varrho_B}{\partial y} \\ = \frac{M^2}{2(M^2 - 1)^{\frac{1}{2}}} \left(\frac{\gamma - 1}{c_s^2 v} \right) \alpha I \end{aligned} \quad (35b)$$

$$\begin{aligned} (M^2 - 1)^{\frac{1}{2}} \frac{\partial \varrho_C}{\partial x} - \frac{\partial \varrho_C}{\partial y} \\ = \frac{M^2}{2(M^2 - 1)^{\frac{1}{2}}} \left(\frac{\gamma - 1}{c_s^2 v} \right) \alpha I. \end{aligned} \quad (35c)$$

The solution to (35a) can be obtained by a simple quadrature in the x -direction. The solutions to (35b) and (35c) are obtained by integrating along characteristics. In general, the characteristics will not always

intersect grid points. The values of source and density at points where characteristics cut mesh lines can be determined by linear interpolation, however, from values expressed at grid points. This is the basis for Carlson's method [18] which we have employed to solve (35b) and (35c). Two cases must be distinguished depending on whether the characteristics cut grid lines parallel to the x -axis or parallel to the y -axis. Let us drop the subscript on ϱ_A and ϱ_B , and let $\varrho_j^l = \varrho(j\Delta x, l\Delta y)$. If it is assumed that $v < 0$, then the difference equations for (35b) and (35c) can be summarized as follows

$$\begin{aligned} \text{For } (M^2 - 1)^{\frac{1}{2}} \frac{\Delta y}{\Delta x} \geq 1, \\ \varrho_{j-1}^{l \pm 1} = \varrho_j^l \frac{\Delta x / \Delta y}{(M^2 - 1)^{\frac{1}{2}}} + \varrho_j^{l \pm 1} \left[1 - \frac{\Delta x / \Delta y}{(M^2 - 1)^{\frac{1}{2}}} \right] \\ - \frac{\Delta x}{2(M^2 - 1)^{\frac{1}{2}}} \left\{ S_{j-1}^{l \pm 1} + \left[1 - \frac{\Delta x / \Delta y}{(M^2 - 1)^{\frac{1}{2}}} \right] S_j^{l \pm 1} \right. \\ \left. + \frac{\Delta x / \Delta y}{(M^2 - 1)^{\frac{1}{2}}} S_j^l \right\}. \end{aligned} \quad (36a)$$

$$\begin{aligned} \text{For } (M^2 - 1)^{\frac{1}{2}} \frac{\Delta y}{\Delta x} < 1, \\ \varrho_{j-1}^{l \pm 1} = \varrho_j^l \left(\frac{\Delta y}{\Delta x} \right) (M^2 - 1)^{\frac{1}{2}} + \varrho_{j-1}^l \left[1 - \frac{\Delta y}{\Delta x} (M^2 - 1)^{\frac{1}{2}} \right] \\ - \frac{1}{2} \Delta y \left\{ S_{j-1}^{l \pm 1} + \left[1 - \frac{\Delta y}{\Delta x} (M^2 - 1)^{\frac{1}{2}} \right] S_{j-1}^l \right. \\ \left. + \frac{\Delta y}{\Delta x} (M^2 - 1)^{\frac{1}{2}} S_j^l \right\}, \end{aligned} \quad (36b)$$

$$S(x, y) = \frac{M^2}{2(M^2 - 1)^{\frac{1}{2}}} \left(\frac{\gamma - 1}{c_s^2 v} \right) \alpha I. \quad (37)$$

In (36a)–(37) the + sign refers to (35b) for ϱ_B and the – sign to (35c) for ϱ_C .

Figures 8a and 8b show the steady-state isodensity contours and the density distribution on the x -axis for a heat source with a Gaussian shaped distribution ($1/e$ intensity radius is 25 units) and an $M = 0.875$ wind blowing in the positive x -direction. Units of time and length are selected so that $c_s = 1$. Solutions were obtained using (30) and (31) and employing the buffer region previously described.

In order to test the effect of the periodic boundary conditions on the steady-state solution the time-dependent Equations (22) were solved using a com-

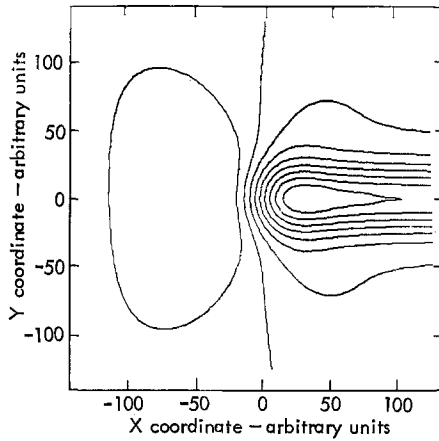


Fig. 8a. Steady-state calculation of isodensity contours for Gaussian source, Mach 0.875 wind

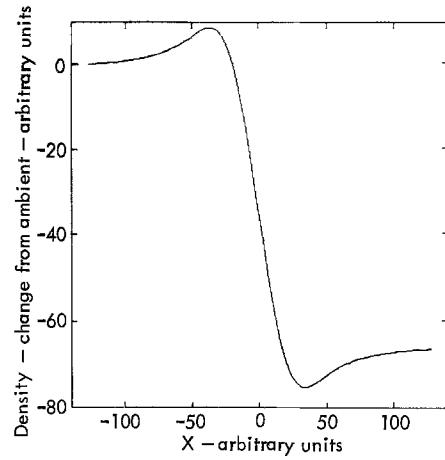


Fig. 8b. On-axis ($y=0$) density profile for steady state calculation. Beam center indicated by $x=0$

bined Laplace transform and DFT (see Appendix C). In the time-dependent calculation a buffer the same size was employed, but no effective way was found to truncate the solution in the buffer region without causing objectionable discontinuities to appear in solution derivatives. The solution was therefore allowed to periodically “wrap around” with the understanding that the solution would become meaningless at a given point with the arrival of the first influence of the periodic boundary condition.

Figure 9a shows the isodensity contours for the time-dependent calculation at $t=320$. Note that the “equilibration” time $a/|c_s - v| = 200$ in these units. If $t = r/|c_s \pm v|$ is taken as a criterion for steady-state conditions the steady state should be well established downstream and to within a distance $1.5a$ upstream

of the origin. The two sets of contours (8a), (9a) compare well where steady-state conditions prevail. Figure 9b shows the density distribution on the x -axis including the buffer for the time-dependent case at $t=320$. Figures 9b and 8b agree on the location of the downstream minimum and the upstream maximum. The difference between the upstream maximum and the downstream minimum is about 7% lower in the steady-state case than in the transient case. (The density difference is what is important since the steady-state solution involves an arbitrary integration constant.) This difference is reasonable since steady state conditions have not advanced very far upstream in the transient case.

Figure 10a shows the steady-state isodensity contours for a $1.5-M$ wind and Figure 10b exhibits the steady-

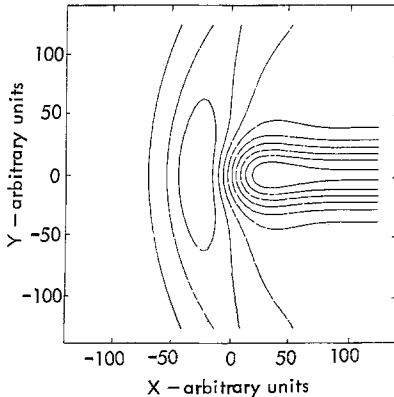


Fig. 9a. Time-dependent calculation of isodensity contours. Same source and Mach 0.875 wind as for Figure 8

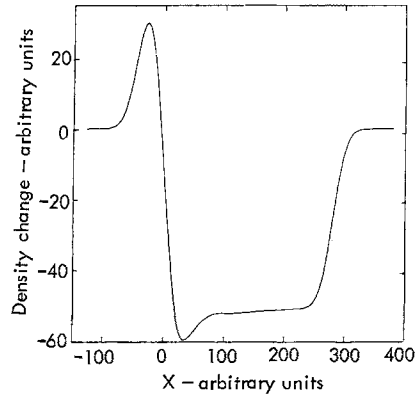


Fig. 9b. On-axis (x -axis) density distribution corresponding to Figure 9a. Beam center indicated by $x=0$

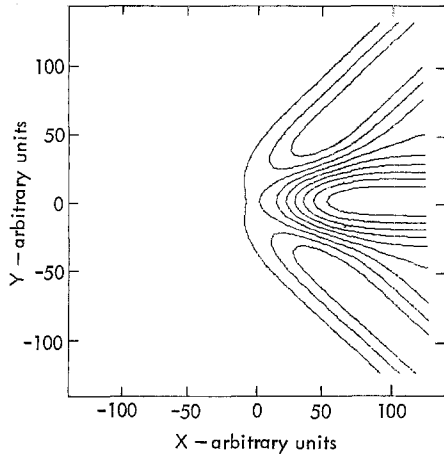


Fig. 10a. Steady-state calculation of isodensity contours for Mach number = 1.5

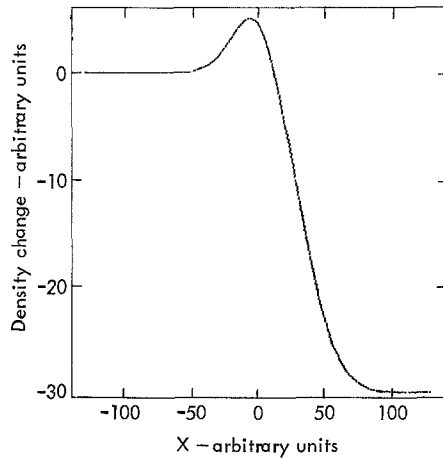


Fig. 10b. On-axis density distribution from steady state calculation for Mach number = 1.5. Beam center indicated by $x=0$

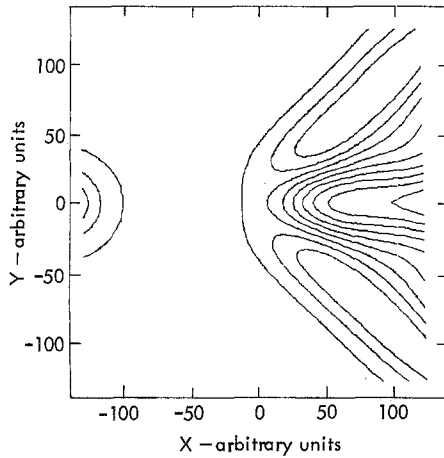


Fig. 11a. Time-dependent calculation of isodensity contours for $M = 1.5$

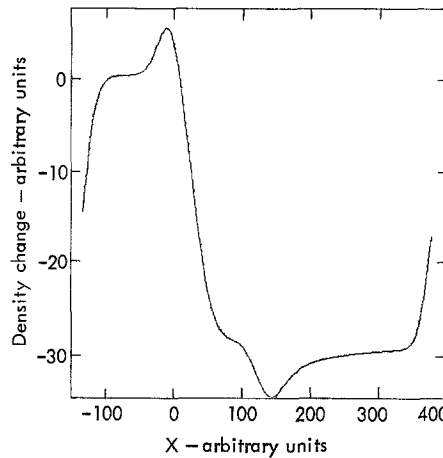


Fig. 11b. Time-dependent calculation. On-axis density dependence for $M = 1.5$. Beam center at $x = 0$

state density distribution along the x -axis. Figures 11a and b are the comparable figures for the transient case at $t = 256$. The contours in Figures 10a and 11b compare very well. The density values between $x = \pm 50$ are also in good agreement.

3. Time-Dependent Isobaric Density Changes

On a time scale of the order $t \lesssim a/v$ the assumption of a steady-state is invalid, and it is necessary to calculate density changes with a time-dependent hydrodynamic model. Provided that $v \ll c_s$, it is adequate to use the isobaric model represented by

(25), which we repeat here as

$$\frac{\partial \varrho_1}{\partial t} + v \frac{\partial \varrho_1}{\partial x} = f(x, y, t), \quad (38a)$$

$$f(x, y, t) = \frac{(\gamma - 1)}{c_s^2} \alpha I. \quad (38b)$$

Equations (38), which describe the density conditions in a stagnation zone, could be solved by integrating along characteristics using Carlson's method. We have chosen a finite Fourier series method of solution, however, because it is potentially more accurate than the Carlson method and because of interest in applying Fourier methods to fluid dynamics problems in general. Let us represent both ϱ_1 and f in terms of

finite Fourier series

$$\varrho_1 = \sum_{n=-\frac{N}{2}+1}^{N/2} \varrho_n(t) e^{\frac{2\pi i n x}{L}}, \quad (39a)$$

$$f = \sum_{n=-\frac{N}{2}+1}^{N/2} f_n(t) e^{\frac{2\pi i n x}{L}}, \quad (39b)$$

where for simplicity we have omitted the variable y . Substitution of expressions (39) into (38) yields, on account of the orthogonality of the basis functions $\exp(2\pi i n x/L)$,

$$\frac{\partial \varrho_n}{\partial t} + \frac{2\pi i n v}{L} \varrho_n = f_n(t). \quad (40)$$

This has the solution for $t = \Delta t$

$$\varrho_n = \varrho_n(0) e^{-\frac{2\pi i n v \Delta t}{L}} + \int_0^t f_n(t') e^{-\frac{2\pi i n v}{L}(t-t')} dt'. \quad (41)$$

If $f_n(t)$ is assumed piecewise linear, $\varrho_n(t^{n+1})$, where $t^{n+1} = t^n + \Delta t$, can be written

$$\begin{aligned} \varrho_n(t^{n+1}) &= \varrho_n(t^n) e^{-\frac{2\pi i n v \Delta t}{L}} + A_n f_n(t^n) \\ &\quad + B_n f(t^{n+1}), \end{aligned} \quad (42)$$

where

$$\begin{aligned} A_n &= \frac{1}{(2\pi i n v / L)} \\ &\cdot \left[\left(\frac{-2\pi i n v \Delta t}{L} \right) - \frac{1-e^{-\frac{2\pi i n v \Delta t}{L}}}{(1-e^{-\frac{2\pi i n v \Delta t}{L}})} \right] \end{aligned} \quad (43a)$$

$$B_n = \frac{1}{(2\pi i n v / L)} \left[1 - \left(\frac{1-e^{-\frac{2\pi i n v \Delta t}{L}}}{(1-e^{-\frac{2\pi i n v \Delta t}{L}})} \right) \right]. \quad (43b)$$

For a source function $f(x, y, t)$ that is confined in both wave-number and configuration space and that varies linearly with time, a solution based on (39), (42) and (43) should be "exact" at sampled mesh points. There is, however, a restriction to be observed in the evaluation of (42). The exponential $\exp(2\pi i n v \Delta t / L)$ when multiplying a DFT will create an inverse DFT which is translated in the x direction according to $x \rightarrow x + v \Delta t$, provided

$$v \Delta t = n \Delta x, n = 0, 1, 2, \dots, N-1. \quad (44)$$

For $v \Delta t$ not an integral multiple of Δx , the exponentials in (42) and (43) will cause the transformed function $\varrho_1(x, t)$ to ring in an undesirable manner.

An additional consequence of this translation is that the portion of the solution located within the strip $L - v \Delta t < x \leq L$ will move into the strip $0 \leq x < v \Delta t$, on account of the periodicity of the Fourier representation (39). This form of aliasing can be eliminated by adding a buffer region. To make this buffer the problem mesh is lengthened in the x -direction to $(2^{N'})L$, where N' is a positive integer. Following each integration step the solution within the buffer region is set to 0. This portion of $\varrho_1(x, t)$ will thus not be able to translate across $x=0$ during the next integration step, provided that $v \Delta t$ is less than or equal to the length of the buffer region. The periodic length L used in (39)–(43) must of course be replaced by L' which includes the length of the buffer. We have chosen a buffer length equal to L , so that time-dependent solutions can be obtained for values of $v \Delta t$ up to and including L . For $v \Delta t$ exceeding this value the code automatically goes into the steady-state hydrodynamic routine described in the previous section. The variable ϱ_1 is real so its double-length real transform is equivalent to a single complex transform of length N , when the buffer length is L .

In general the condition (44) will not be met. This situation can be remedied in two ways. First $v \Delta t$ can be rounded to the nearest integral value $n \Delta x$ before evaluating the exponentials in (42) and (43). A more exact procedure is to represent the exponential in (42) and (43) by a weighted average

$$e^{\frac{i 2\pi n v \Delta t}{L}} \approx f e^{\frac{i 2\pi n n_1}{L}} + (1-f) e^{\frac{i 2\pi n (n_1+1)}{L}}, \quad (45)$$

where n_1 is the greatest integer less than $v \Delta t / \Delta x$, and f is given by

$$f = (v \Delta t - n_1 \Delta x) / \Delta x. \quad (46)$$

The solution (42) will thus involve at most one linear interpolation of the source and one of the dependent variables ϱ_1 at the previous time for a given value of x . The Carlson method, in contrast, can involve many linked linear interpolations for x -values far downstream, if $v \Delta t \gg \Delta x$.

Equations (39)–(43) will be appropriate for determining the transient density behavior due to air heating by a cw laser. A slight modification of this treatment is required for the density changes induced by multipulse laser heating. This will be the subject of the next section.

4. Density Changes Induced by Multi-Pulse Laser Heating

Isobaric or “steady state” density changes induced by multi-pulse heating are governed by the equation

$$\begin{aligned} \frac{\partial \varrho_1^{mp}}{\partial t} + v \frac{\partial \varrho_1^{mp}}{\partial x} \\ = - \frac{(\gamma-1)}{c_s^2} \alpha \sum_n \tau I_n(x, y) \times \delta(t - t_n), \end{aligned} \quad (47)$$

where $I_n(x, y)$ represents the average intensity of the n th pulse and τ is a pulse duration chosen so that τI_n represents the pulse fluence. The presence of the δ -functions is justified by the fact that the pulse durations are short in comparison with the time required to establish pressure equilibrium. Let Δt = the time interval between successive pulses.

The solution to (47) at $t = n\Delta t$ can be written

$$\begin{aligned} \varrho_1^{mp}(x, y, n\Delta t) &= \varrho_1^{mp}(x - v\Delta t, y, (n-1)\Delta t) \\ &- \frac{(\gamma-1)}{c_s^2} \alpha \tau I(x, y), \end{aligned} \quad (48)$$

where it is understood that

$$\varrho_1^{mp}(x, y, t) = 0 \text{ for } x \text{ on upwind boundary.} \quad (49)$$

Equation (48), which includes the contribution of the n th pulse, is used to update ϱ_1^{mp} following the arrival of each pulse at the axial position z . It is incorrect, however, to include the contribution of the n th pulse to ϱ^{mp} in calculating $\delta\varepsilon(\varrho_1)$, since there is no time within a pulse duration for a steady-state density distribution to develop. Instead one should evaluate $\delta\varepsilon(\varrho_1)$ using the expression

$$\varrho_1(x, y, n\Delta t) = \varrho_1^{mp}(x - n\Delta t, y, (n-1)\Delta t) + \varrho_1^{sp}, \quad (50)$$

where ϱ_1^{sp} is the density contribution obtained by solving the complete set of linearized hydrodynamic equations with the n th pulse as a heat source. The contribution ϱ_1^{sp} leads to “self-blooming” of the pulse and ideally should be calculated along with the propagation, in a self-consistent manner, by utilizing many sampling times within the pulse. This type of detailed calculation is impractical for the multi-pulse propagation calculation envisaged here. However, one can do the self-blooming calculation in a self-consistent way if but one time is needed to represent the pulse, i.e. the pulse is triangular in time. This turns out to be a good approximation for moderate blooming.

We can obtain the Fourier transform of the density change resulting from heating by a triangular pulse from expression (C19) in Appendix C by setting $v=0$ and $\tilde{b}=0$

$$\begin{aligned} \tilde{\varrho}_1^{sp} &= - \frac{\tilde{a}}{c_s^2} \left\{ \frac{\tau^2}{2} + \frac{\cos[c_s \tau(k_x^2 + k_y^2)^{\frac{1}{2}}] - 1}{c_s^2 (k_x^2 + k_y^2)} \right\} \\ &= - \frac{(\gamma-1)\alpha \tilde{I}\tau}{2c_s^2} \\ &\cdot \left\{ 1 - \frac{\sin^2 \left[\frac{1}{2} c_s \tau (k_x^2 + k_y^2)^{\frac{1}{2}} \right]}{\left[\frac{1}{2} c_s \tau (k_x^2 + k_y^2)^{\frac{1}{2}} \right]^2} \right\}. \end{aligned} \quad (51)$$

This same result can be obtained by assuming a square shape in time and averaging over the pulse history. From (C19) we obtain on setting $v=0$ and $\tilde{a}=0$

$$\begin{aligned} \tilde{\varrho}_1^{sp} &= - \frac{\tilde{b}}{c_s^2} \left\{ t - \frac{\sin[c_s (k_x^2 + k_y^2)^{\frac{1}{2}} t]}{c_s (k_x^2 + k_y^2)^{\frac{1}{2}}} \right\} \text{ and} \\ \frac{1}{\tau} \int_0^\tau \tilde{\varrho}_1^{sp} dt &= - \frac{(\gamma-1)\alpha \tilde{I}\tau}{2c_s^2} \\ &\cdot \left\{ 1 - \frac{\sin^2 \left[\frac{1}{2} c_s \tau (k_x^2 + k_y^2)^{\frac{1}{2}} \right]}{\left[\frac{1}{2} c_s \tau (k_x^2 + k_y^2)^{\frac{1}{2}} \right]^2} \right\}. \end{aligned} \quad (52)$$

The computation of the term ϱ_1^{sp} in (50) requires the evaluation of the inverse Fourier transform of $\tilde{\varrho}_1^{sp}$, which in turn can be approximated by the DFT

$$\begin{aligned} \varrho_1^{sp}(j\Delta x, k\Delta y) &= (2N)^{-2} \\ &\cdot \sum_{m,n=-N+1}^N \tilde{\varrho}_1^{sp} \left(\frac{2\pi n}{L}, \frac{2\pi m}{L} \right) e^{\frac{2\pi i(mj+nk)}{2N}}. \end{aligned} \quad (53)$$

The basis functions used in the DFT (53) are periodic on a square of side $2L$ which allows for a buffer region extending an additional distance L in both the x and y directions from the region of interest. To avoid aliasing of periodic “wrap-around” effects τ must satisfy the restriction $c_s \tau \leq L$.

There is, however, an additional source of possible aliasing; i.e. the nonlinear $\delta\varepsilon E$ term in the wave equation that is proportional to $\delta\varrho E$. Fourier components in ϱ_1^{sp} and E having wave vectors exceeding $2\pi n/L$ in magnitude, where $n > N/4$, can lead through this nonlinearity to Fourier components in both variables that are outside the range of possible description by the available mesh.

In the solution of the propagation equation in conjunction with (25) for calculating the transient blooming properties of cw beams, aliasing has never been a problem; the shorter Fourier components are not generated in the density by (42) if they are not already present in the laser intensity. In the case of pulse blooming, however, the source term for the hydrodynamic equations is proportional to $\nabla^2 I$, whose Fourier transform is $(k_x^2 + k_y^2)\tilde{I}$. Thus there is a tendency to magnify short-wave components in ϱ_1^{sp} , and aliasing can become a problem. In problems run to date where pulse blooming was important the aliasing was eliminated by the application of either a hard filter, in which case all Fourier components of ϱ_1 are set to 0 if either $|k_x|$ or $|k_y| \geq N\pi/2L$, or a soft filter,

which involves multiplying (51) by

$$F(k_x, k_y) = \frac{1}{1 + [(k_x^2 \Delta x^2 + k_y^2 \Delta y^2)f^2]^{n/2}} \quad (54)$$

before applying the inverse transform. The use of $f=0.5$ and $n=8$ in (54) has yielded good results.

Figures 12 and 13 show comparisons of single-pulse blooming calculated using the triangular pulse model and the more detailed model described in Section 7. In both cases an initial Gaussian beam with a $1/e^2$ radius of 15 cm and peak intensity of 6 MW/cm^2 is assumed to be focused at a distance of 4.5 km. The wavelength is $10.6 \mu\text{m}$ and the absorption coefficient is $0.25 \times 10^{-5} \text{ cm}^{-1}$. The values of τ are 30 μs and 50 μs for Figures 12 and 13, respectively.

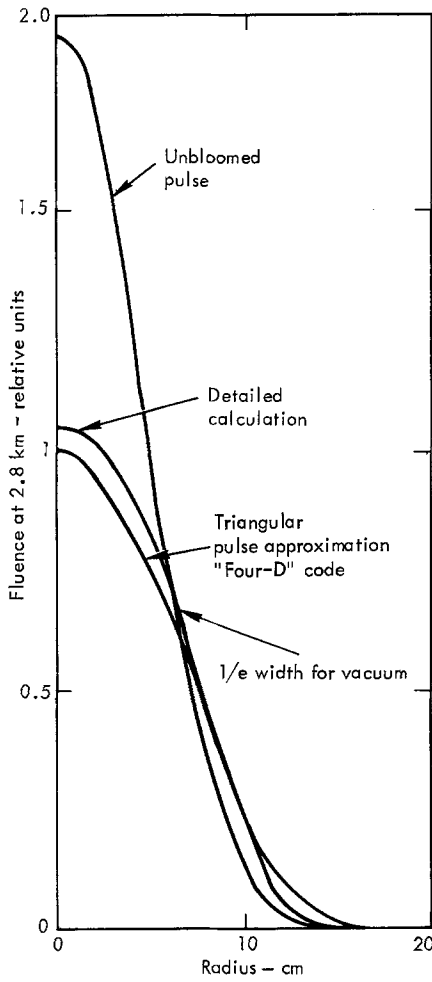


Fig. 12. Comparison of calculated thermal blooming using triangular pulse model and detailed calculation with many time values. Pulse duration is assumed to be 30 μs

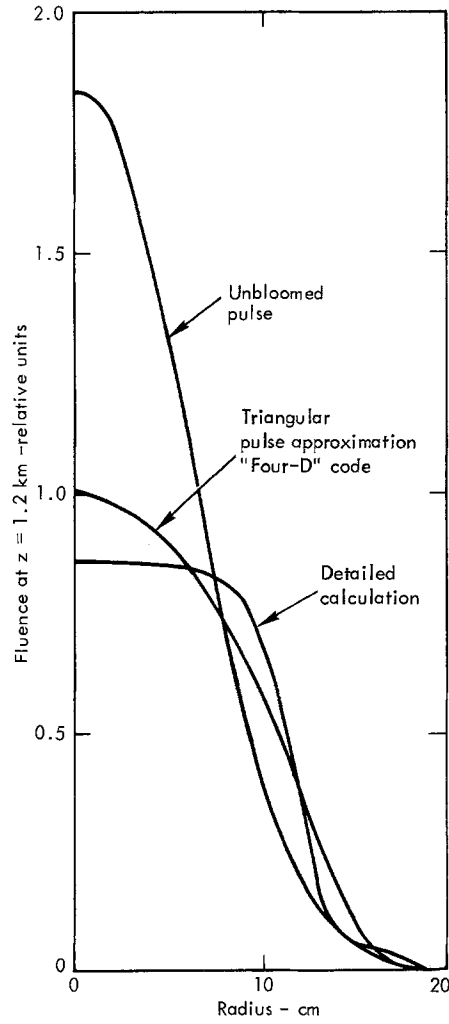


Fig. 13. Comparison of calculated thermal blooming using triangular pulse model and detailed calculation. Pulse duration is 50 μs

In the detailed model calculation the pulse shape is Gaussian in time with the width adjusted to give the same total energy as the triangular pulse. Plotted in Figures 12 and 13 is the intensity averaged over pulse history, which is proportional to the fluence. Also plotted for comparison is the unbloomed pulse shape corrected for linear absorption. In the case of Figure 12 and $\tau = 30 \mu\text{s}$ the propagation is to a distance of 2.8 km and the blooming is moderate. Agreement between the triangular pulse and the detailed model is reasonably good regarding both beam shape and peak intensity.

In the case of Figure 13 and $\tau = 50 \mu\text{s}$ the propagation is only to a distance of 1.2 km and the blooming is quite pronounced. The beam shapes in the triangular pulse and detailed model are slightly different. The peak intensities for the two cases differ by 10%, but the intensity averaged over the area containing one half of the power agrees for both cases to within 1%.

In conclusion, the triangular-pulse characterization is certainly a reasonable one in the absence of detailed waveform information for specific multipulse devices and should be useful in defining the limits to multipulse devices imposed by pulse self-blooming.

5. Treatment of Atmospheric Turbulence

The effect of thermally induced density changes over the propagation path from z^n to $z^n + \Delta z$ is taken into account in the propagation calculation by computing at each position z^n a phase shift $k\Gamma(x, y)$, see (4), (5), where

$$\Gamma(x, y) = \int_{z^n}^{z^n + \Delta z} \delta n(x, y, z) dz. \quad (55)$$

with $\delta n = \delta \varepsilon / 2$.

Bradley [6] has developed a numerical treatment of turbulence whereby a contribution $\Gamma_{\text{turb}}(x, y)$ in the form of (55) resulting from turbulent density fluctuations is added to the phase shift created by the laser heating of the atmosphere. The phase change $\Gamma_{\text{turb}}(x, y)$ is calculated by a Monte Carlo technique that simulates the statistical nature of δn in a turbulent atmosphere [19]. This "phase screen" description of atmospheric turbulence has also been studied in some detail by Brown [7], and it is the one that we have employed.

For a homogeneous turbulent atmosphere one can write the correlation function for Γ as

$$\begin{aligned} R_{\Gamma\Gamma}(\mathbf{r}_t - \mathbf{r}'_t) &= \int_{z^n}^{z^n + \Delta z} dz \int_{z^n}^{z^n + \Delta z} dz' \langle n(\mathbf{r}) n(\mathbf{r}') \rangle \\ &= \int_{z^n}^{z^n + \Delta z} dz \int_{z^n}^{z^n + \Delta z} dz' \int_{-\infty}^{\infty} e^{-ik_x|x-x'|} dk_x \\ &\quad \cdot \int_{-\infty}^{\infty} e^{-ik_y|y-y'|} dk_y \int_{-\infty}^{\infty} e^{-ik_z|z'-z|} dk_z \\ &\quad \cdot \Phi_n(k_x, k_y, k_z) dk_z, \end{aligned} \quad (56)$$

where \mathbf{r}_t is a position vector in the transverse plane, and $\Phi_n(k_x, k_y, k_z)$ is the spectral density for the index fluctuations. We make the usual assumption of a von Karman spectrum, which specifies that

$$\Phi_n = 0.033 C_n^2 (k_0^2 + k_x^2 + k_y^2 + k_z^2)^{-1/6}. \quad (57)$$

Here C_n^2 is the index structure constant, and $k_0 = 2\pi/L_0$, where L_0 is the outer scale length. Carrying out the integrations first over z and z' in (56), one obtains

$$\begin{aligned} \int_{z^n}^{z^n + \Delta z} dz \int_{z^n}^{z^n + \Delta z} dz' e^{-ik_z|z'-z|} &= \frac{2}{k_z^2} (1 - \cos k_z \Delta z) \\ &+ \left[\frac{2\Delta z}{ik_z} + \frac{2i}{k_z^2} \sin k_z \Delta z \right]. \end{aligned} \quad (58)$$

The bracketed part of (58) can be ignored because $\Phi_n(k_x, k_y, k_z)$ is an even function of k_z . In the limit of z large in comparison with L_0 we can use the relation

$$\frac{2}{k_z^2} (1 - \cos k_z \Delta z) \cong 2\pi \Delta z \delta(k_z). \quad (59)$$

Hence for sufficiently large Δz Equation (56) reduces to

$$\begin{aligned} R_{\Gamma\Gamma}(x - x', y - y') &= \int_{-\infty}^{\infty} dk_x e^{-ik_x|x-x'|} \\ &\quad \cdot \int_{-\infty}^{\infty} dk_y e^{-ik_y|y-y'|} \Phi_n(k_x, k_y, 0). \end{aligned} \quad (60)$$

Generalizing the one-dimensional approach of Brown [7], we assume for $\Gamma(x, y)$ the expression

$$\begin{aligned} \Gamma(x, y) &= \int_{-\infty}^{\infty} dk_x e^{ik_x x} \int_{-\infty}^{\infty} dk_y e^{ik_y y} a(k_x, k_y) \\ &\quad \cdot \Phi_n^{\frac{1}{2}}(k_x, k_y), \end{aligned} \quad (61)$$

where $\Phi_n(k_x, k_y) = \Phi_n(k_x, k_y, 0)$ and where $a(k_x, k_y)$ is a two-dimensional complex random function with the property

$$a(k_x, k_y) = a^*(-k_x, -k_y), \quad (62)$$

Equation (62) follows from the fact that $\Gamma(x, y)$ must be a real function. We further take $a(k_x, k_y)$ in the form

$$a(k_x, k_y) = \frac{a'(k_x, k_y) + ia''(k_x, k_y)}{\sqrt{2}}, \quad (63)$$

where it is assumed that

$$\langle a'(k_x, k_y) a''(k'_x, k'_y) \rangle = 0 \quad (64a)$$

$$\begin{aligned} \langle a'(k_x, k_y) a'(k'_x, k'_y) \rangle &= \delta(k_x - k'_x) \\ &\cdot \delta(k_y - k'_y) + \delta(k_x + k'_x) \delta(k_y + k'_y) \end{aligned} \quad (64b)$$

$$\begin{aligned} \langle a''(k_x, k_y) a''(k'_x, k'_y) \rangle &= \delta(k_x - k'_x) \\ &\cdot \delta(k_y - k'_y) - \delta(k_x + k'_x) \delta(k_y + k'_y). \end{aligned} \quad (64c)$$

The symmetry and anti-symmetry of the right-hand members of (64b) and (64c) is dictated by the relation (62) which requires that

$$a'(k_x, k_y) = a'(-k_x, -k_y) \quad (65a)$$

$$a''(k_x, k_y) = -a''(-k_x, -k_y). \quad (65b)$$

Thus $a'(k_x, k_y)$ must exhibit mirror symmetry and $a''(k_x, k_y)$ mirror antisymmetry. If a' and a'' are specified for the upper half plane, for example, then they are also specified for the lower half-plane by (65). It should be noted that the choice of $a(k_x, k_y)$ real would impose an unjustifiable four-quadrant symmetry on $\Gamma(x, y)$.

We may summarize conditions (64) and (65) as follows

$$\begin{aligned} \langle a(k_x, k_y) a(k'_x, k'_y) \rangle &= \frac{1}{2} \{ \langle a'(k_x, k_y) a(k'_x, k'_y) \rangle - \langle a''(k_x, k_y) a''(k'_x, k'_y) \rangle \} \\ &= \frac{1}{2} \{ \delta(k_x - k'_x) \delta(k_y - k'_y) + \delta(k_x + k'_x) \delta(k_y + k'_y) \\ &\quad - \delta(k_x - k'_x) \delta(k_y - k'_y) + \delta(k_x + k'_x) \delta(k_y + k'_y) \} \\ &= \delta(k_x + k'_x) \delta(k_y + k'_y). \end{aligned} \quad (66)$$

If we now calculate the correlation function R_{TT} , using expression (61) and (66), we obtain

$$\begin{aligned} \langle \Gamma(x, y) \Gamma(x', y') \rangle &= \int_{-\infty}^{\infty} \int_{-\infty}^{\infty} \int_{-\infty}^{\infty} \int_{-\infty}^{\infty} dk_x dk_y dk'_x dk'_y \\ &\cdot \delta(k_x + k'_x) \delta(k_y + k'_y) \\ &\cdot \Phi_n^{\frac{1}{2}}(k_x, k_y) \Phi_n^{\frac{1}{2}}(k'_x, k'_y) e^{i(k_x x + k_x' x')} e^{i(k_y y + k_y' y')} \\ &= \int_{-\infty}^{\infty} \int_{-\infty}^{\infty} dk_x dk_y e^{i(k_x |x - x'| + k_y |y - y'|)} \Phi_n(k_x, k_y), \end{aligned} \quad (67)$$

which is precisely the desired expression (60).

The numerical computation of (61) requires that the spectrum of $\Phi_n(k_x, k_y)$ be made finite, in both x and y directions. If a trapezoidal evaluation of the double integral is performed, $\Gamma(x, y)$ may be calculated from the double sum

$$\begin{aligned} \Gamma(n_x \Delta x, n_y \Delta y) &= \frac{2\pi}{N} \left(\frac{0.033\pi \Delta z C_n^2}{\Delta x \Delta y} \right)^{1/2} \\ &\cdot \sum_{n_x=-N+1}^N \sum_{n_y=-\frac{N}{2}+1}^{\frac{N}{2}} \frac{\exp\left(\frac{i\pi n_x}{N} + \frac{2\pi i n_y}{N}\right)}{\left[\left(\frac{2\pi L}{L_0}\right)^2 + \left(\frac{2\pi n_y}{N}\right)^2 + \left(\frac{\pi n_y}{N}\right)^2\right]^{11/12}} \\ &\cdot [a'(n_x, n_y) + ia''(n_x, n_y)] \end{aligned} \quad (68)$$

which may be evaluated by a sequence of FFT operations. Note that we have made $\Gamma(x, y)$ periodic with a period $2L$ in the x -direction. A buffer of length L allows us to translate the resulting phase screen with the wind as long as $v\Delta t \leq L$. For $v\Delta t > L$ the phase screen begins to repeat itself.

An alternative code option allows for the selection of an entirely new phase screen for each successive time value. The independent random numbers $a'(n_x, n_y)$ and $a''(n_x, n_y)$ are assumed to obey Gaussian statistics and to have variance 1. They are generated by selecting a pseudo-random number, scaling it, reducing it to an integer, and executing a table look up. Only numbers for the upper half-plane are chosen in this fashion. Values for a' and a'' in the lower half-plane are obtained using (65a) and (65b).

In general, every z -position will require the generation of a statistically independent phase screen. This is to be expected since Δz has been assumed large in comparison with L_0 . If L_0 is in fact larger than Δz , the phase screens at successive z -positions will not be statistically independent and the approximation (59) cannot be used. A more accurate evaluation of the z -integrations in (56) will yield [20]

$$\Phi_n(x, y) = \frac{0.033 C_n^2}{(k_0^2 + k_x^2 + k_y^2)^{11/6}} f(\alpha) \quad (69a)$$

$$f(\alpha) = \frac{\alpha + 0.714588\alpha^2}{1.875 + 1.3236\alpha + 0.718012\alpha^2} \quad (69b)$$

$$\alpha^2 = \frac{(\Delta z)^2}{4} (k_0^2 + k_x^2 + k_y^2). \quad (69c)$$

Expressions (69) are the ones actually used in evaluating the sum (68) although one may question the validity of the independent phase screen concept for $\Delta z \leq L_0$.

Figures 14a–c and Figures 15a–c show a comparison of the isodensity contours at various positions along the propagation path on the way to a focus at 2.5 km for a thermally bloomed beam calculated with and without turbulence. The wavelength is assumed to be $3.8 \mu\text{m}$ and slewing of the beam results in effective wind speeds varying between 25 and 40 m/s. The index

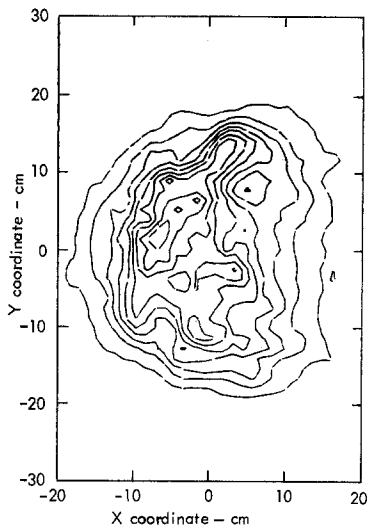


Fig. 14a. Isointensity contours for thermal blooming in the presence of turbulence, nearfield

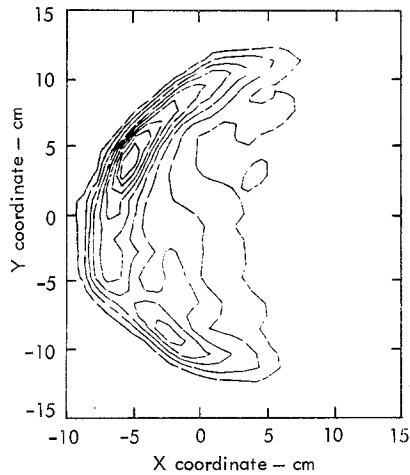


Fig. 14b. Isointensity contours for thermal blooming in the presence of turbulence. Close to focus

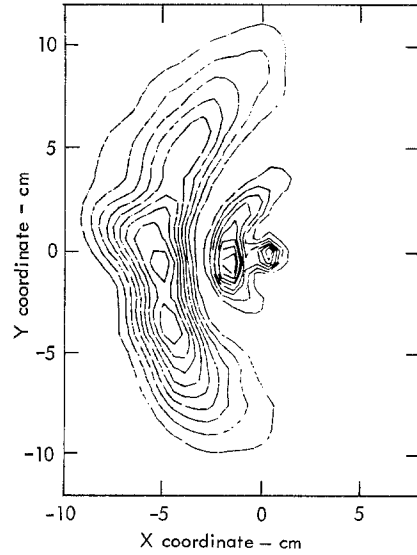


Fig. 14c. Isointensity contours for thermally bloomed pulse in the presence of turbulence. In the focal plane

structure constant C_n^2 is assumed to have the value $1.25 \times 10^{-15} \text{ m}^{-2/3}$, which is characteristic of moderate turbulence. The notable feature of the turbulent contours is the tendency for image reconstruction to take place in the focal plane. A long-time-average characterization of the beam in the presence of turbulence would, of course, require an average over an ensemble of realizations with different random number sets.

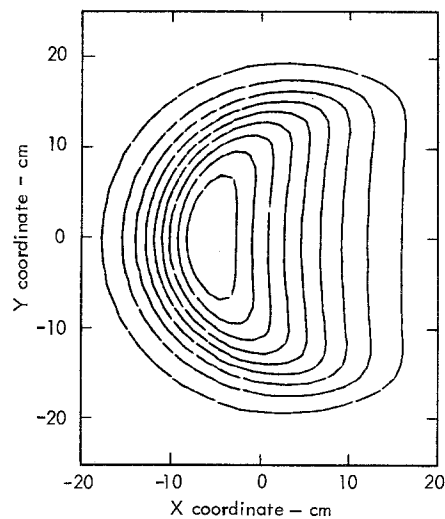


Fig. 15a. Isointensity contours for thermally bloomed pulse without turbulence. Same conditions as Figure 14a

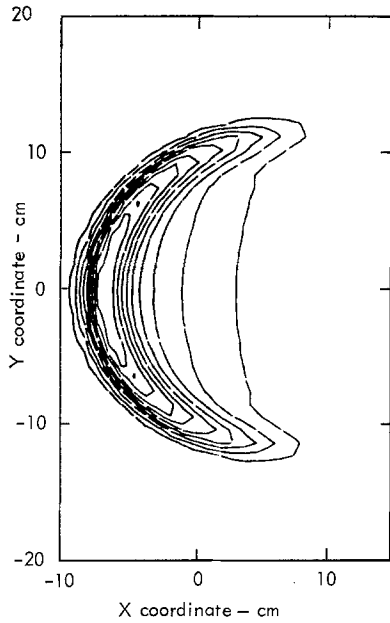


Fig. 15b. Isointensity contours for blooming without turbulence.
See Figure 14b

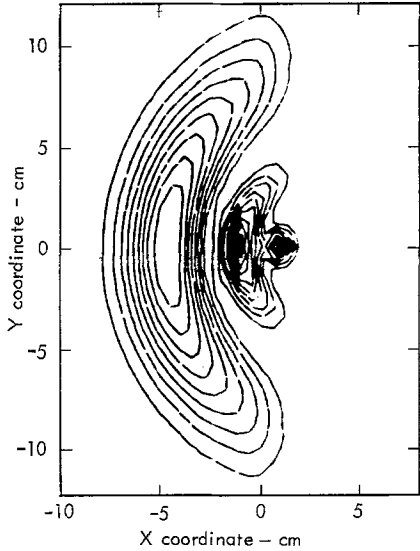


Fig. 15c. Isointensity contours for blooming without turbulence.
See Figure 14c

6. Single-Pulse Thermal Blooming

The single-pulse thermal blooming code used to check the triangular pulse approximation model described in Section 4 is based on a solution of the nonlinear hydrodynamic equations along with (1), the propagation in cylindrically symmetrical ($r-z$) ge-

ometry. The hydrodynamic equations are the following

$$\frac{\partial \varrho}{\partial t} + \frac{1}{r} \frac{\partial}{\partial r} (\varrho v r) = 0, \quad (70a)$$

$$\frac{\partial}{\partial t} (\varrho v) + \frac{1}{r} \frac{\partial}{\partial r} (\varrho v^2 r) = - \frac{\partial}{\partial r} (P + Q), \quad (70b)$$

$$\frac{\partial W}{\partial t} + \frac{1}{r} \frac{\partial}{\partial r} [rv(W+P+Q)] = \alpha |\mathcal{E}|^2. \quad (70c)$$

In (70) ϱ , v , and P represent the total density, velocity, and pressure, W is the total internal plus kinetic energy density, and Q is an artificial viscosity that is important only when shocks are present. In (70) the usual approximation is made of omitting z -dependence. This is an excellent approximation since all axial gradients are completely negligible in comparison with radial gradients.

The hydrodynamic equations are integrated using a variant of the implicit continuous-fluid Eulerian [21], (ICE) method, which eliminates the Courant stability condition when shocks are absent. The propagation equation is integrated using an implicit cubic-spline technique [10], which guarantees the radial continuity of the gradient and Laplacian of the laser field \mathcal{E} . For maximum efficiency, the code automatically varies both temporal and spatial integration step sizes in order to insure a prescribed level of accuracy.

Figures 16 to 21 indicate in somewhat greater detail the nature of the pulse thermal blooming for the focused 30 μ s and 50 μ s pulses described briefly in Section 4 [22]. Figures 16 and 17 are three-dimensional plots of the density and laser intensity as functions of radius and time at a distance of 3 km from the laser. The plots begin at the time when the maximum on-axis intensity is achieved. Figures 18–20 refer to the stronger-blooming case of the 50 μ s pulse at a distance of 1.2 km. Figures 18 and 19 are three-dimensional plots of the density and intensity respectively. Figure 20 contains radial-intensity profiles at consecutive times spaced at 3.33 μ s intervals starting at the time of maximum on-axis intensity. Figure 21a shows the half-fluence radius—the radius at which the fluence drops to one half its peak value—as a function of propagation distance for the 30 μ s pulse, the 50 μ s pulse, and a pulse that undergoes no blooming. The apparent saturation in the behavior of the half-fluence radius for the 50- μ s pulse results from the tendency of the large hole in the rear of the pulse to

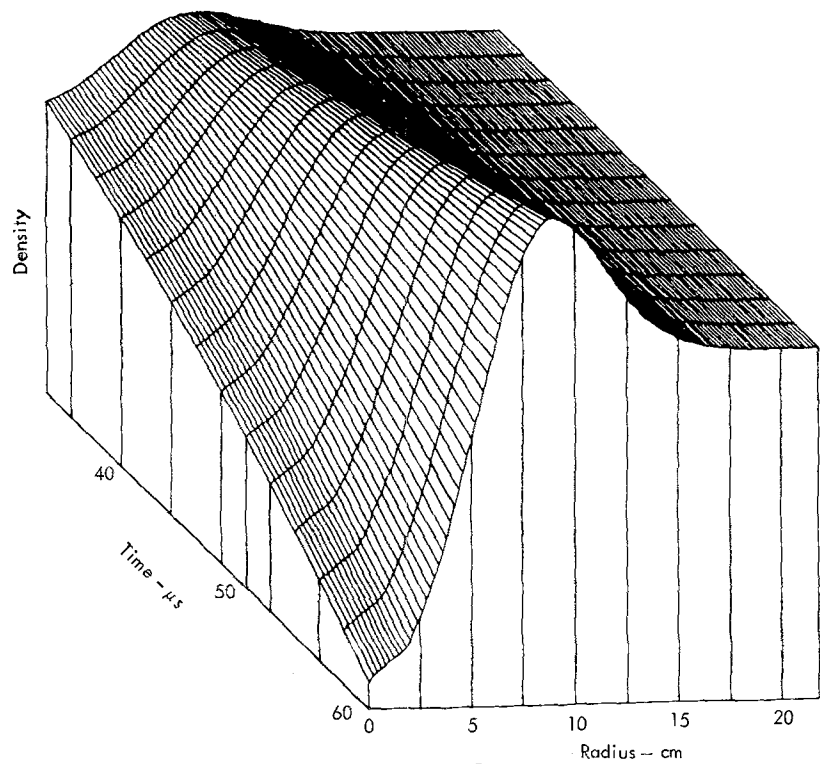


Fig. 16. Three-dimensional plot of density that accompanies the thermally bloomed pulse vs time and radius. Distance is 3 km and pulse duration is 30 μ s

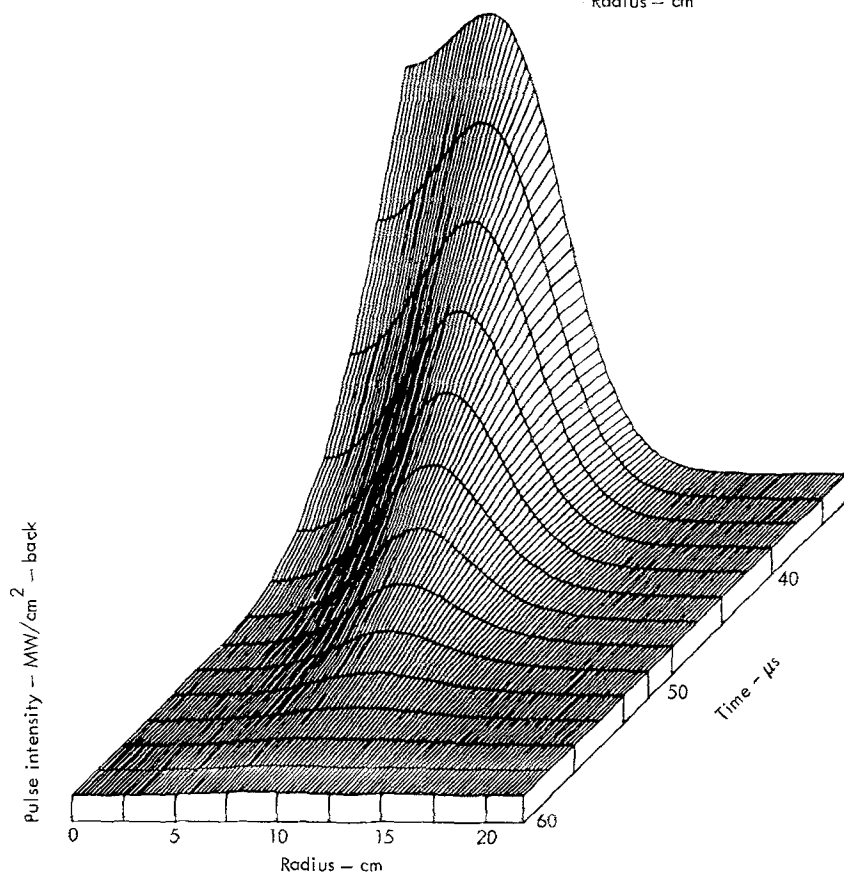


Fig. 17. Three-dimensional plot of intensity vs time and radius. Same conditions as Figure 16

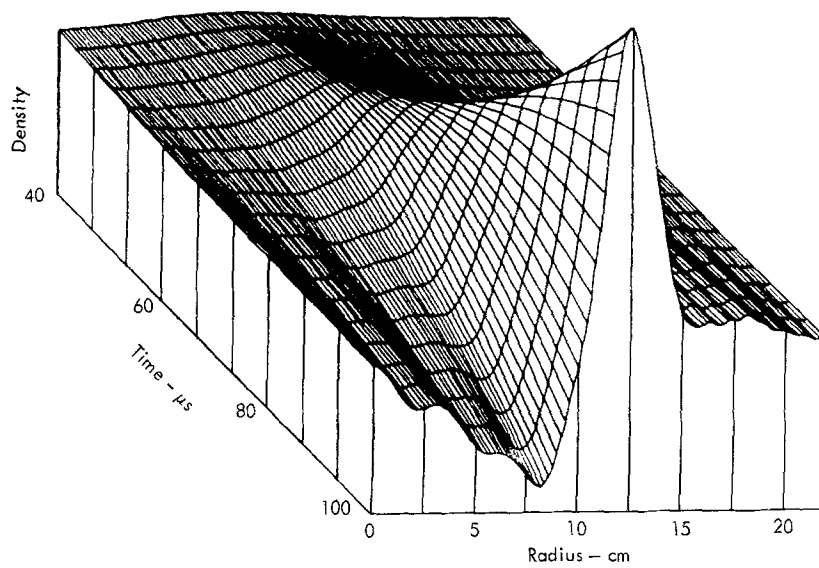


Fig. 18. Three-dimensional plot of density vs time and radius. Pulse duration is 50 μs and distance is only 1.2 km

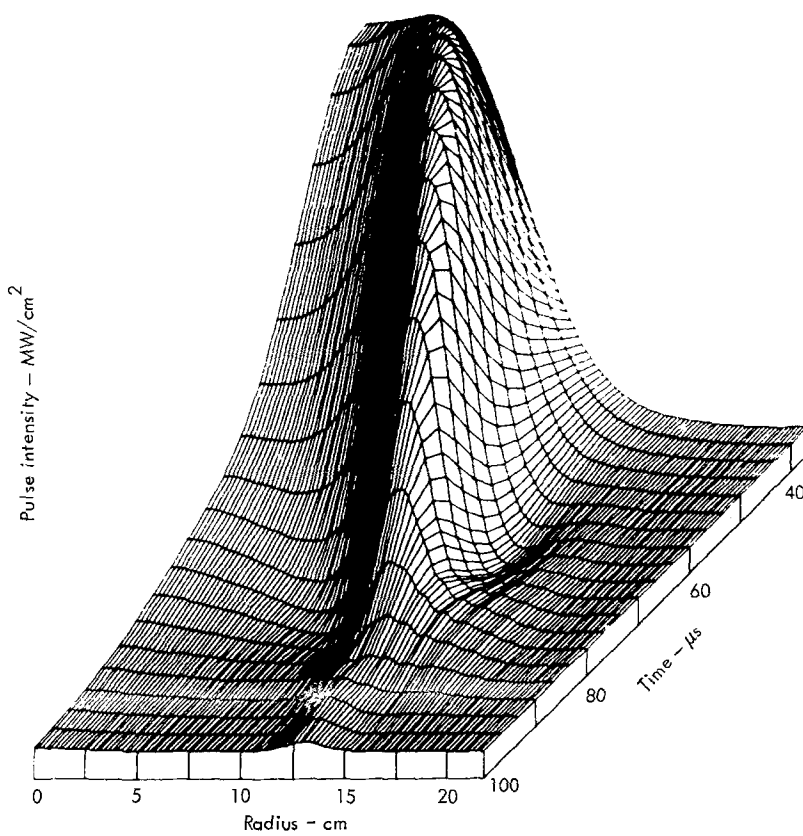


Fig. 19. Three-dimensional plot of intensity vs time and radius. Same conditions as Figure 18

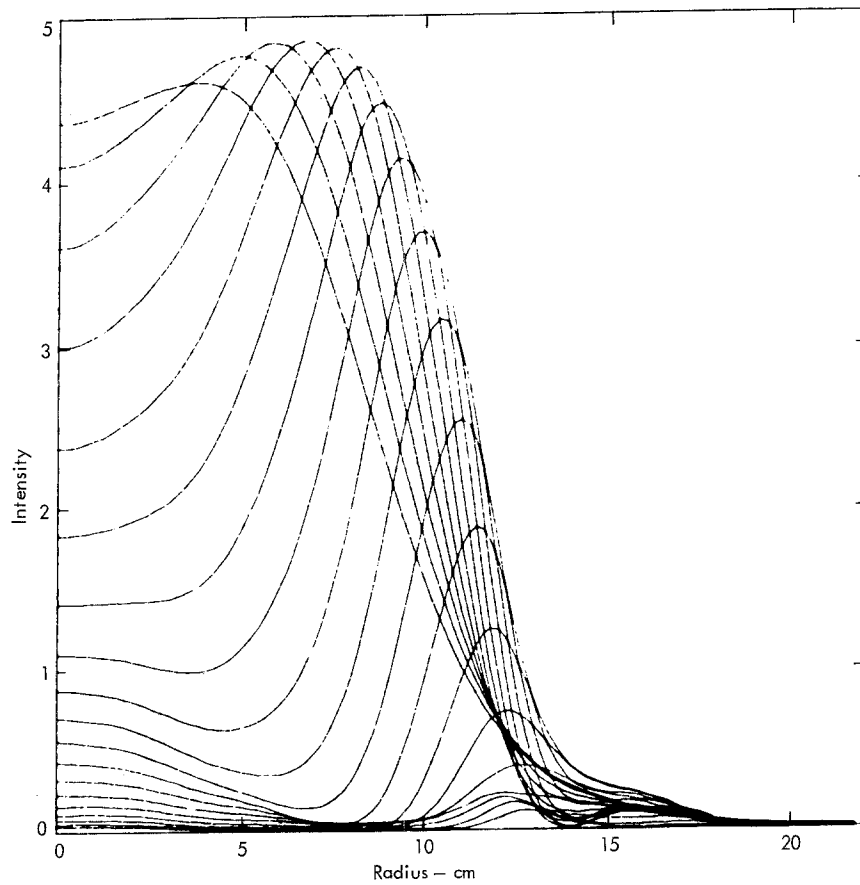


Fig. 20. Radial intensity profiles for consecutive times in pulse. Same conditions as Figure 19

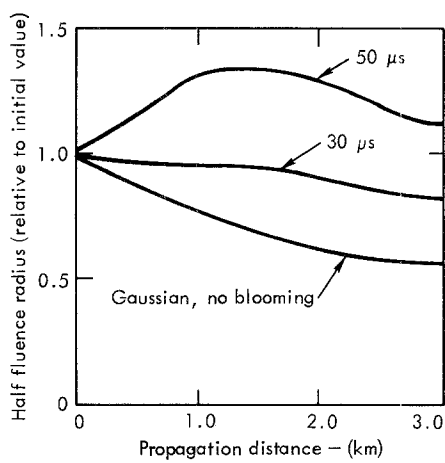


Fig. 21a. Comparison of "half-fluence" radius as a function of range for 30 μ s, 50 μ s, and unbloomed Gaussian pulses

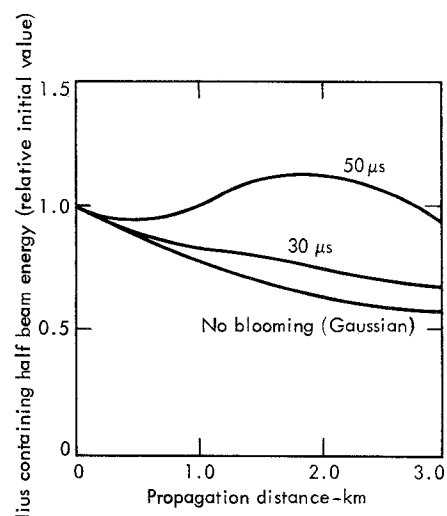


Fig. 21b. Comparison of radius containing one half of beam energy as a function of range for the three pulses of Figure 21a

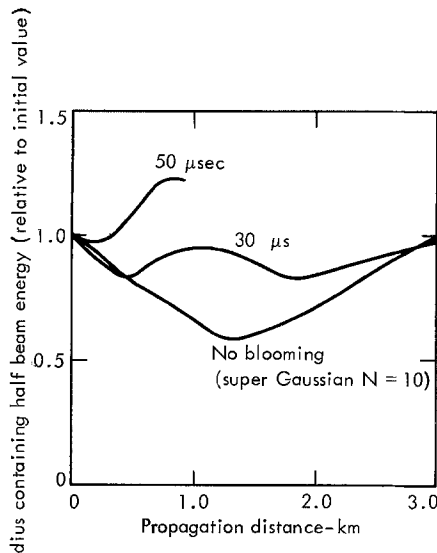


Fig. 21c. Comparison of radius containing one half of beam energy for "super-Gaussian" beam shape and various pulse durations, with $N = 10$ and $a = 10.6$ cm

fill in with time due to diffraction. This effect, in turn, smoothes out the density pattern and reduces density gradients and further refraction.

Figure 21b shows the dependence on z of the radius containing one half of the total pulse energy, which is a measure of the average beam power. Figure 21c shows the behavior of the same radius variable for a beam that is initially super-Gaussian in shape, $\exp \left[-\left(\frac{r}{a} \right)^N \right]$, with $N = 10$ and $a = 10.6$ cm. Such a beam has a nearly flat intensity distribution at the start, which might be thought to minimize thermal blooming since the density gradients across the beam are minimized. In actual fact, however, diffraction redistributes the beam energy and the resulting blooming is actually substantially greater than for the Gaussian-shaped beams described in Figures 21a and b.

7. Transonic Slewing

The sonic point, where $v = c_s$, is a singular point for the linearized hydrodynamic equations [23], but due to the motion of a weak shock upwind from the source the sound speed in the heated medium is raised above that of the undisturbed medium and so Mach 1 conditions are never actually attainable. The steady-state density conditions can nonetheless be

obtained by applying the linearized hydrodynamic equations with the correct upstream sound speed. This suggests that one may obtain information about propagation under transonic conditions by solving the linearized hydrodynamic equations along the entire propagation path, avoiding the transonic point, but coming as close as possible to it. This calculation is similar to Bradley's [9], but it also takes account of the beam propagation.

Figures 22–27 show the results of propagating a laser beam through a transonic zone in this manner with the transonic zone occurring about halfway to the target. The assumed values of α and λ are 0.25×10^{-5} cm $^{-1}$ and 10.6 μm, respectively. The laser and target are moving at speeds of 15 m/s and 690 m/s, respectively, in the same direction with no background wind. The effective transverse wind speed resulting from slewing is shown in Figure 28. The laser is focused on target at $z = 1$ km. The effective wind speed reaches Mach 1 at $z = 488.50$ m for $c_s = 345$ m/s.

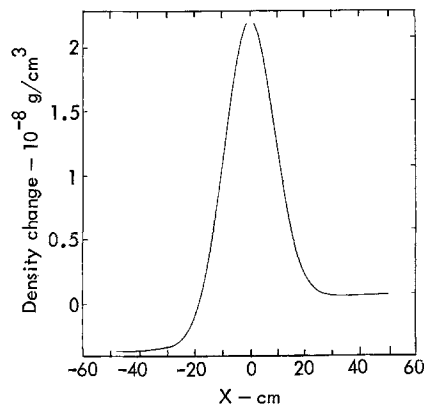


Fig. 22. On-axis density profile for $M = 1.003$

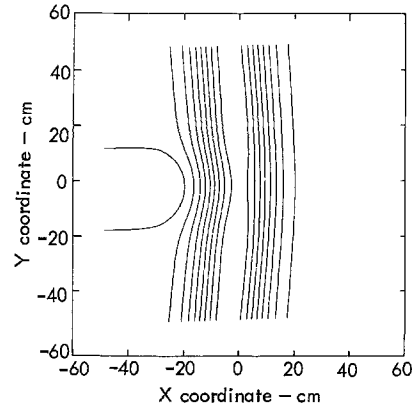
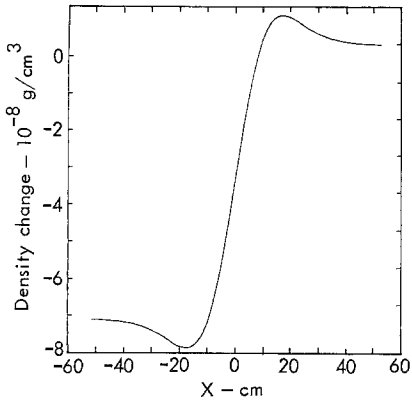
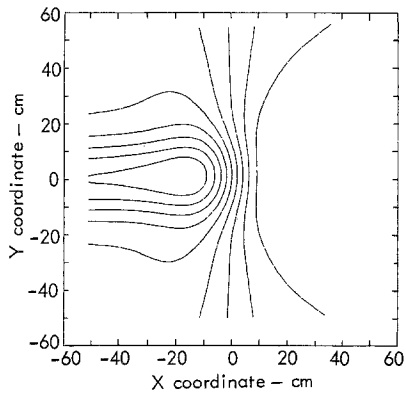
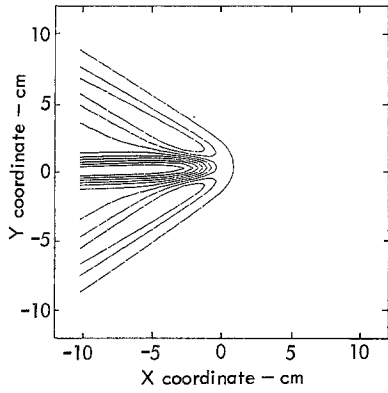


Fig. 23. Isodensity profiles for $M = 1.003$

Fig. 24. On-axis density profile for $M = 0.94$ Fig. 25. Isodensity profiles for $M = 0.94$, same conditions as for Figure 24Fig. 26. Isodensity profiles close to target for $M = 1.95$

In order to treat the transonic region with sufficient accuracy, the propagation path was broken into three segments: from $z=0$ to $z=456.59$ m, from $z=456.59$ m to 520.53 m, and from 520.53 m to 1 km. The beam

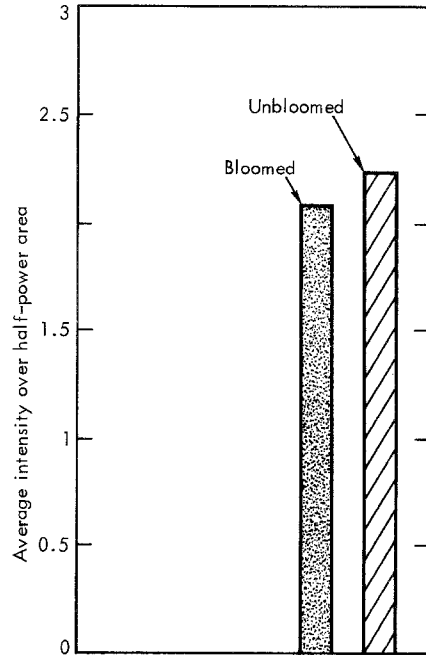


Fig. 27. Comparison of bloomed and unbloomed intensities at target after transonic slewing. Sonic point halfway to target

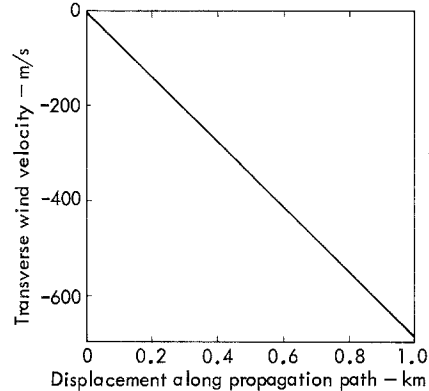


Fig. 28. Transverse wind velocity vs range used in transonic blooming scenario. Sonic point is somewhere near half-way to target

was propagated over the “transonic” or middle segment in 20 equally spaced steps of 3.1965 m. One of these steps lands on the sonic point at $z=488.5$ m. Since the density calculation is actually centered midway between the propagation z-steps, the Mach number on which it is based never becomes 1, although it comes extremely close to that value. In fact the closest M comes to 1 is 1.003 at $z=490.15$ m. Figures 22 and 23 show the density profile along the x axis and the isodensity contours for this value of z .

Figures 24 and 25 show the x -axis density profile and the isodensity contours at $z=458.19$ m where $v=324.52$ m/s and $M=0.94$. Figure 26 shows the isodensity contours close to the target and Figure 27 indicates a comparison of the bloomed beam at the target with one propagated through vacuum and corrected for linear absorption. Clearly the amount of blooming is insignificant.

Blooming is enhanced somewhat when the sonic point occurs at the target. Figure 29 shows the blooming at the target for the wind velocity vs propagation distance shown in Figure 30. Figures 31 and 32 show the x -dependence of density along the x axis and the

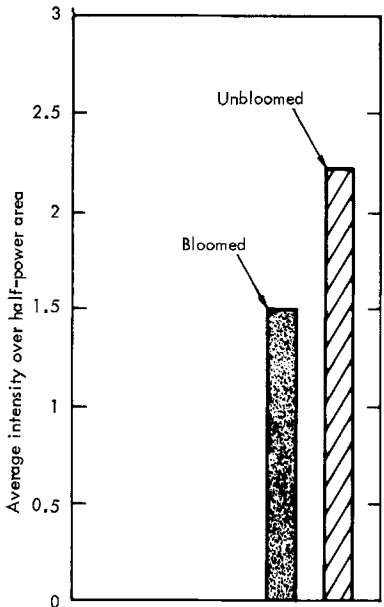


Fig. 29. Comparison between bloomed and unbloomed intensities at target when sonic point is right on target

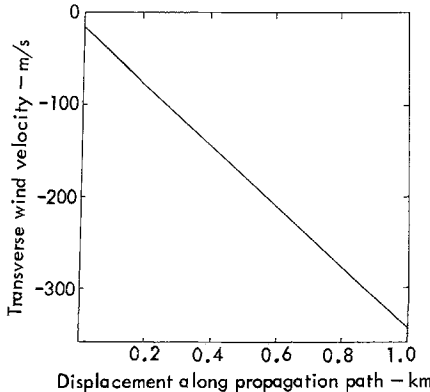


Fig. 30. Transverse wind speed vs propagation distance for scenario in which sonic point occurs right at target in focal plane

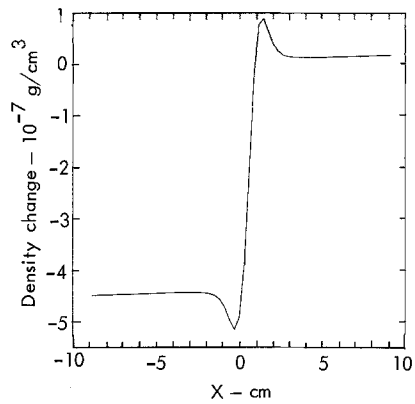


Fig. 31. On-axis density variation with x at target for $M=0.997$

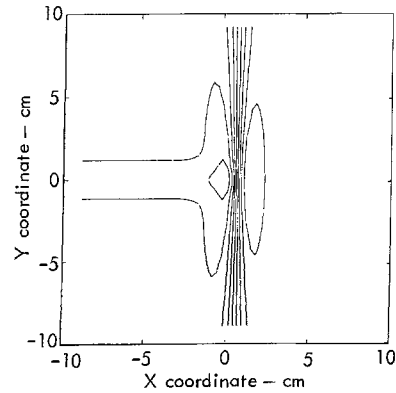


Fig. 32. Isodensity contours on target, conditions same as for Figures 29–31

isodensity contours at a position close to the target. Clearly the density changes are greater than for the case when the transonic zone occurs near the middle of the propagation path.

8. Propagation of cw Laser Beams Through Stagnation Zones

Beam slewing combined with laser platform motion can under certain conditions lead to a null value of the effective transverse wind speed at some point along the propagation path. The portion of the beam path over which the effective wind speed is negligible is referred to as a stagnation or dead zone. Without forced convection to remove the heated air relatively large density changes may arise, causing gross beam distortions in the focal plane. This problem was first recognized by Hayes [24] who formulated an analytic theory of the phenomenon. This analysis indicated that the effect could be serious, particularly if the dead

zone were located near the target. The dead zone problem was investigated using a simplified numerical model by Hogge [25].

Recently the effects of dead zones on laser beam propagation were measured experimentally by Berger et al. by passing a laser beam through a pivoted absorption cell filled with CO₂ [26, 27]. The first set of these experiments was performed with the absorption cell in a horizontal position. In these experiments natural convection flow played a role in the resulting thermal blooming. The effects of natural convection were eliminated in a second set of experiments by orienting the absorption cell vertically and allowing the laser beam to enter the cell at the bottom. It is to this set of experiments that we now turn our attention. The experimental configuration is shown in Figure 33. The parameters used in the calculation were as follows

Absorbing medium: (CO₂ at 10 atm pressure)

$$\alpha = 4.2 \times 10^{-3} \text{ cm}^{-1}$$

$$c_s = 267 \text{ m/s}$$

$$\gamma = 1.304$$

$$\frac{n-1}{\varrho_0} = 0.4584$$

$$\varrho_0 = 0.01964 \text{ g/cm}^3.$$

Laser: CO₂ at 10.6 μm wavelength

Power = 7.4 W

Gaussian beam with e⁻¹ radius = 0.35 cm at cell input

Geometry:

$$z_f = 100.625 \text{ cm}$$

$$\text{Cell length} = 97.5 \text{ cm}$$

Numerical details: problem run with 20 time values, Δt = 5 ms.

In these experiments the laser beam was turned on by opening an iris. This resulted in an on-axis beam intensity measured in the focal plane which increased as

$$I(r=0) \sim (1 - e^{-t/t_r}). \quad (71)$$

No attempt was made to model this time-dependent diffraction problem. Instead the source intensity was turned on according to (71), with a value of t_r = 2 ms, while the beam shape was maintained constant.

The absorption cell in the experiment was enclosed with flat windows. For angles of incidence other than normal, refraction at the windows causes the beam to shift laterally from the assumed axial position. In the experiment the beam was monitored in a position where the intensity was a rapidly varying function of lateral position. Therefore in comparing calculated axial intensities with measured values, a correction must be applied to take account of this refraction-induced shift.

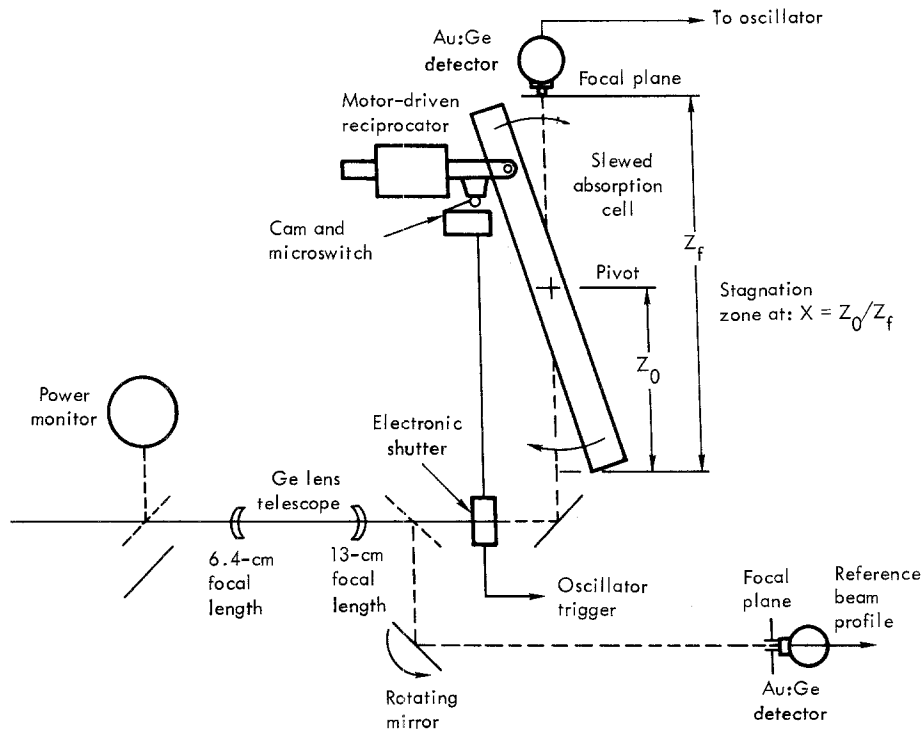


Fig. 33. Experimental arrangement used in [26]

The actual measured beam was approximately Gaussian at the focus with an e^{-1} radius of 750 μm , in the absence of an absorption cell. A diffraction-limited Gaussian beam, on the other hand, would focus to a e^{-1} radius of 460 μm for a 10.6 μm wavelength. This apparent non-diffraction-limited behavior could be modeled in two ways, neither of which would be satisfactory: e.g. by assuming a longer focal length or by running the problem with a 17.1 μm wavelength. The first option gives an incorrect taper to the beam and the wrong beam waist position. The second option gives poorer results than are obtained by running a diffraction-limited beam with the correct wavelength.

Figures 34–37 show results for the pivot position at $x=z_0/z_f=0.1$ or the dead zone 1/10th the way to the focal plane. Figures 34, 35, and 36 correspond to slew rates of 0.089, 0.178, and 0.222 rad/s, respectively, and

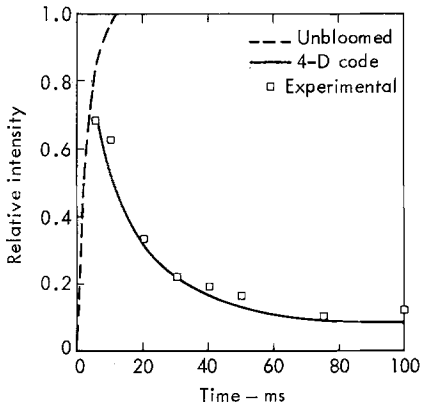


Fig. 34. On-axis intensity vs time, comparison of calculated and measured values. In this and in subsequent figures, the refraction at cell window has been taken into account. $\lambda=10.6 \mu\text{m}$, $x=0.1$, $\Omega=0.089 \text{ rad/s}$

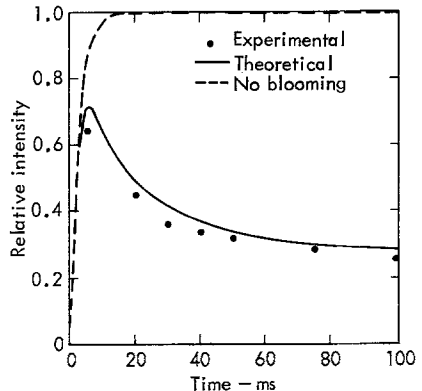


Fig. 35. On-axis intensity vs time, $\lambda=10.6 \mu\text{m}$, $x=0.1$, $\Omega=0.178 \text{ rad/s}$

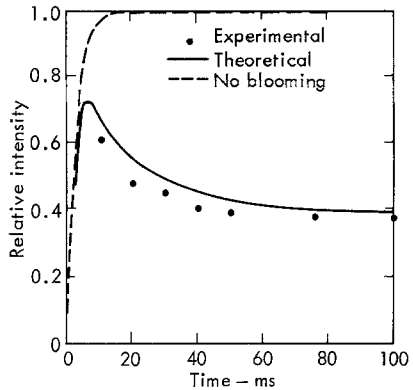


Fig. 36. On-axis intensity vs time $\lambda=10.6 \mu\text{m}$, $x=0.1$, $\Omega=0.222 \text{ rad/s}$

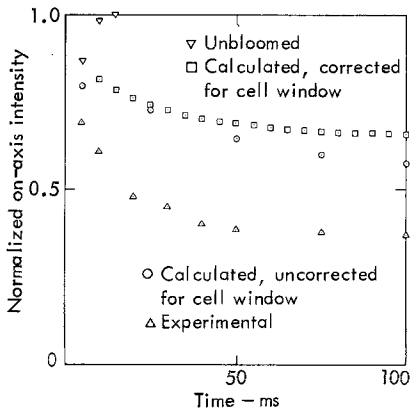


Fig. 37. On-axis intensity vs time, $\lambda=17.1 \mu\text{m}$, $x=0.1$, $\Omega=0.222 \text{ rad/s}$

are calculated for a 10.6 μm wavelength. Plotted is the intensity in the focal plane at a point shifted from the origin in accordance with refraction at the windows of the absorption cell, normalized to the axial intensity in the focal plane if no absorber were present. The calculated results are in reasonably good agreement with the measured values. Figure 37 for a slew rate of 0.222 rad/s has been calculated assuming a wavelength of 17.1 μm , which should give the correct focal spot size in the absence of absorption. The agreement with the experiment is noticeably poorer and the refractive beam shift correction only serves to make matters worse. Figures 38–41, which correspond to Figures 34–37, respectively, show the intensity distribution for $y=0$ plotted as a function of x . Indicated by arrows are the x values that correspond to the experimental axial position.

Figure 42 corresponds to $x=0.48$ and a wavelength of 10.6 μm . Agreement is poor and in particular the theoretical curve does not display a dip. Figure 43

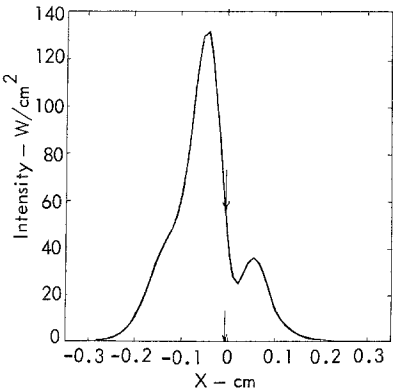


Fig. 38. Dependence of intensity on displacement along wind axis. Conditions are the same as for Figure 34. In this and Figures 39–41 and Figure 43 the arrows indicate the on-axis position corrected for refraction at the cell window

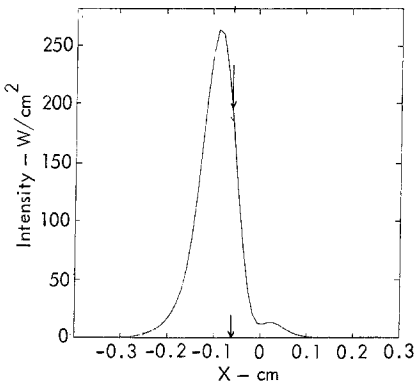


Fig. 39. Dependence of intensity on displacement along wind axis. Conditions are the same as for Figure 35

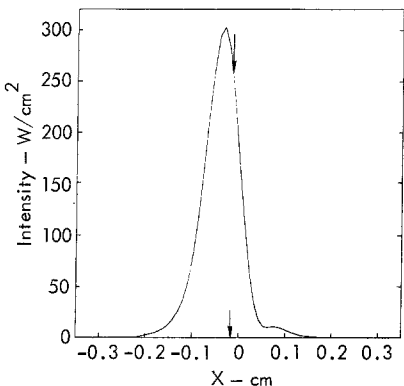


Fig. 40. Dependence of intensity on displacement along wind axis. Conditions are the same as for Figure 36

shows the corresponding intensity distribution along the x axis. The reason for the poorer agreement between experiment and theory in this case is unclear. In particular it is difficult to assess how much im-

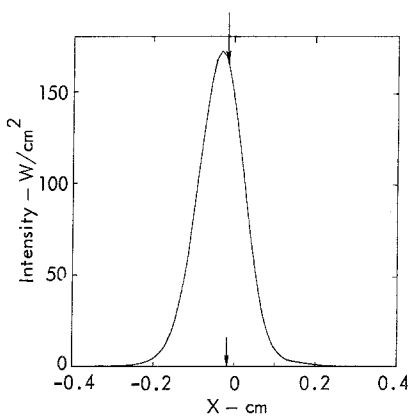


Fig. 41. Dependence of intensity on displacement along wind axis. Conditions are the same as for Figure 37 where $\lambda = 17.1 \mu\text{m}$

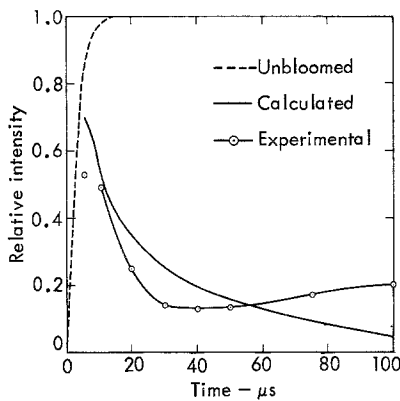


Fig. 42. On-axis intensity vs time, $\lambda = 10.6 \mu\text{m}$, $x = 0.48$, $\Omega = 0.178 \text{ rad/s}$

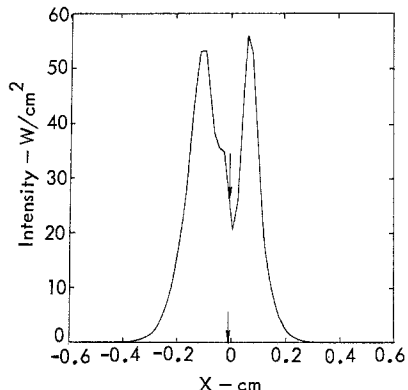


Fig. 43. Dependence of intensity on displacement along wind axis. Conditions are the same as for Figure 42

portance to attach to the inability of the calculation to match the propagation characteristics of the experimental beam in the absence of an absorbing cell.

Acknowledgment. The authors are indebted to C. H. Woods for much of the calculation associated with stagnation zones and for his contributions to the final section of this report, to E. H. Canfield for contributions to the treatment of turbulence and for various helpful suggestions, and to Peter Ulrich and John Hayes for valuable comment and discussion.

References

1. A. H. Aitken, J. H. Hayes, P. B. Ulrich: "Propagation of High Energy 10.6 Micron Laser Beams Through The Atmosphere"; U.S. Naval Research Laboratory, Washington, D. C., Rept. 7293 (1971); P. B. Ulrich, J. H. Hayes, J. H. Hancock, J. T. Ulrich: "Documentation of PROPE, A Computer Program for Propagation of High Power Laser Beams Through Absorbing Media"; U.S. Naval Research Laboratory, Washington, D. C., Rept. 7681 (1974)
2. J. Hermann, L. C. Bradley: "Numerical Calculation of Light Propagation"; MIT Lincoln Laboratory, Cambridge, Mass., Rept. LTP-10 (1971)
3. P. B. Ulrich: "A Numerical Calculation of Thermal Blooming of Pulsed Focused Laser Beams"; U.S. Naval Research Laboratory, Washington, D. C., Rept. 7382 (1971)
4. P. B. Ulrich, J. Wallace, J. Opt. Soc. Am. **63**, 8 (1973)
5. H. Kleiman, K. W. O'Neil, Appl. Phys. Letters **23**, 43 (1973)
6. L. C. Bradley: "Simulation of Atmospheric Index Fluctuations"; Lincoln Laboratory, Cambridge, Mass. (preprint)
7. W. P. Brown, Jr.: "High Energy Laser Propagation"; Hughes Research Laboratory, Rept. on contract N00014-B-C-0460 (1973)
8. A. Edwards: Lawrence Livermore Laboratory, Rept. UCIR-902 (1975)
9. L. C. Bradley: "Thermal Blooming in the Transonic Regime"; MIT Lincoln Laboratory, Cambridge, Mass., Rept. LTP-24 (1974)
10. J. A. Fleck, Jr.: J. Comp. Phys. **16**, 324 (1974)
11. M. D. Feit, J. A. Fleck, Jr.: Bull. Am. Phys. Soc. (Series II) **19**, 962 (1974)
12. An unsymmetrized exponential transformation was used by J. Hermann and L. C. Bradley in [2]
13. V. I. Talanov: JETP Letters **11**, 799 (1970) [ZhETP Pis. Red. **11**, 303 20 (March 1969)]
14. The DFT method of solving the propagation equation is also employed by other workers, e.g. H. J. Breaux: "An Analysis of Mathematical Transformations and a Comparison of Numerical Techniques for Computation of High Energy CW Laser Propagation in an Inhomogeneous Medium"; Ballistic Research Laboratories, Rept. No. 1723 (1974); P. B. Ulrich: In *NRL Optical Radiation Program Progress Report*; U.S. Naval Research Laboratory, Washington, D. C., Memorandum Report 2874 (1974)
15. W. T. Cochran, J. W. Cooley, D. L. Favin, H. D. Helms, R. A. Kaenel, W. W. Lang, G. C. Moling, Jr., D. E. Nelson, C. M. Rader, P. D. Welch: Proc. IEEE **55**, 1664 (1967)
16. A. J. Campillo, J. E. Pearson, S. L. Shapiro, N. J. Terrell, Jr.: Appl. Phys. Letters **23**, 85 (1973)
17. N. J. Terrell, Jr.: Los Alamos Scientific Laboratory, Los Alamos, N. M., private communication (1975)
18. R. D. Richtmyer, K. W. Morton: *Difference Methods for Initial Value Problems*, (Interscience, New York 1967)
19. M. G. Rusbridge: J. Comp. Phys. **2**, 288 (1968)
20. We are indebted to E. H. Canfield, Jr., Lawrence Livermore Laboratory, for these more accurate expressions
21. F. H. Harlow, A. A. Amsden: J. Comp. Phys. **8**, 197 (1971)
22. Results for the thermal blooming of a single collimated pulse are presented in [4]
23. A nonlinear solution for the flow near "Mach = 1" as a function of Mach number has been derived by J. H. Hayes: Appl. Opt. **13**, 2072 (1972)
24. J. N. Hayes: unpublished report, U.S. Naval Research Laboratory, Washington, D. C.
25. C. B. Hogge, R. R. Butts: "Propagation Effects of a Slewed Beam with Transverse Wind Null Spots"; Air Force Weapons Laboratory, Kirkland AFB, N. M., Rept. AFWL-TR-73-76 (1973)
26. R. T. Brown, P. J. Berger, F. G. Gebhardt, H. C. Smith: "Influence of Dead Zones and Transonic Slewing on Thermal Blooming"; United Aircraft Research Laboratory, East Hartford, Conn., Rept. N921724-7 (1974)
27. P. J. Berger, F. G. Gebhardt, D. C. Smith: "Thermal Blooming Due to a Stagnation Zone in a Slewed Beam"; United Aircraft Research Laboratory, East Hartford, Conn., Rept. N921724-12 (1974)

Appendix A

Proof of the Second-Order Accuracy of the Symmetrically Split Operator Solution to the Propagation Equation

Consider for simplicity the equation

$$\frac{\partial \mathcal{E}}{\partial z} = a(z) \mathcal{E} = (\Delta_{\perp} + \chi) \mathcal{E}, \quad (A.1)$$

where Δ_{\perp} is the transverse Laplacian operator. The solution to (A.1) can be expressed formally as

$$\mathcal{E}(z) = \exp \left(\int_0^z a(z') dz' \right), \quad (A.2)$$

where, according to time-dependent quantum mechanical perturbation theory, the exponential Equation (A.2) is taken to mean

$$\begin{aligned} \exp \left(\int_0^z a(z') dz' \right) &= 1 + \int_0^z a(z') dz' + \int_0^z \int_0^{z'} a(z') dz' \int_0^{z''} a(z'') dz'' \\ &\quad + \int_0^z \int_0^{z'} a(z') dz' \int_0^{z''} a(z'') dz'' \int_0^{z'''} a(z''') dz'''. \end{aligned} \quad (A.3)$$

Substituting the operator $a(z)$ as defined in (A.1), one obtains, to second order in z ,

$$\begin{aligned} \exp \left(\int_0^z a(z') dz' \right) &= 1 + \Delta_{\perp} z + \int_0^z \chi(z') dz' + \Delta_{\perp}^2 \frac{z^2}{2} + \Delta_{\perp} \int_0^z dz' \int_0^{z'} \chi(z'') dz'' \\ &\quad + \int_0^z \chi(z') z' \Delta_{\perp} dz' + \int_0^z \chi(z') dz' \int_0^{z''} \chi(z'') dz'' + O(z^3). \end{aligned} \quad (A.4)$$

We can also write to second order in z

$$\begin{aligned} \exp \left(\frac{1}{2} \Delta_{\perp} z \right) \exp \left(\int_0^z \chi(z') dz' \right) \exp \left(\frac{1}{2} \Delta_{\perp} z \right) &= 1 + \Delta_{\perp} z + \Delta_{\perp}^2 \frac{z^2}{2} \\ &\quad + \int_0^{z'} \chi(z') dz' + \int_0^z \chi(z') dz' \int_0^{z'} \chi(z'') dz'' + \nabla_{\perp} \frac{z}{2} \int_0^z \chi(z') dz' \\ &\quad + \frac{z}{2} \int_0^z \chi(z') \Delta_{\perp} dz. \end{aligned} \quad (A.5)$$

Thus we may write

$$\begin{aligned} \exp \left[\int_0^z a(z') dz' \right] &= \exp \left(\frac{1}{2} A_{\perp} z \right) \exp \left[\int_0^z \chi(z') dz' \right] \exp \left(\frac{1}{2} A_{\perp} z \right) \\ &- A_{\perp} \int_0^z dz' \left[\frac{z}{2} \chi(z') - \int_0^{z'} \chi(z'') dz'' \right] - \int_0^z dz' \chi(z') \left(\frac{z}{2} - z' \right) A_{\perp} + O(z^3). \end{aligned} \quad (\text{A.6})$$

In order for the expression (A.5) to be a representation for (A.3) to second order, the integral terms on the right-hand side of (A.6) must either vanish or be of third order. Clearly they vanish if $\chi(z)$ is a constant. If $\chi(z)$ can be represented as a Taylor series in z

$$\chi(z) = \chi(0) + \chi'(0)z + \chi''(0)z^2 + \dots \quad (\text{A.7})$$

they are $O(z^3)$ as required. In one important case, however $\chi(z)$ cannot be represented as a power series, namely, the case in which $\chi(z) \sim a + bz^{1/2}$. In this case the integral terms are $O(z^{5/2})$. An important example of this behavior is $\Gamma_{\text{turb}}(\Delta z)$ defined in (61), which scales as $z^{1/2}$.

Clearly the importance of using the symmetrized operator form (A.5) in solving the propagation problem increases as the number of propagation steps in the calculation diminishes.

If

$$\begin{aligned} z_x &= z_y = z_f \\ z_1 &= z_2 = \frac{z}{1 - (z/z_f)} \end{aligned} \quad (\text{B.7})$$

and (B.4) becomes (9) or

$$\mathcal{E}(x, y, z) = \frac{1}{1 - \frac{z}{z_f}} \mathcal{E}' \left(\frac{x}{1 - \frac{z}{z_f}}, \frac{y}{1 - \frac{z}{z_f}}, \frac{z}{1 - \frac{z}{z_f}} \right) e^{i \frac{k(x^2 + y^2)}{2(z_f - z)}}. \quad (\text{B.8})$$

In the more general case where $z_x \neq z_y$, expression (B.4) is best evaluated in terms of its transverse Fourier transform. We then have

$$\mathcal{E}(x, y, z) = \frac{1}{\left(1 - \frac{z}{z_x} \right)^{\frac{1}{2}} \left(1 - \frac{z}{z_y} \right)^{\frac{1}{2}}} \mathcal{E}'' \left(\frac{x}{1 - \frac{z}{z_x}}, \frac{y}{1 - \frac{z}{z_y}}, z \right) e^{i \frac{k}{2} \left(\frac{x^2}{z_x - z} + \frac{y^2}{z_y - z} \right)}. \quad (\text{B.9})$$

where

$$\tilde{\mathcal{E}}''(k_x, k_y, z) = \tilde{\mathcal{E}}''(k_x, k_y, 0) e^{i \left(\frac{z_1 k_x^2}{2k} + \frac{z_2 k_y^2}{2k} \right)} \quad (\text{B.10})$$

Equation (B.10) now represents a generalization of (15).

Appendix B

Derivation of Talanov Lens Transformation for Cylindrical Phase Fronts

In this appendix we derive a lens transformation capable of compensating for the more general phase front represented by the expression

$$\frac{k}{2} \left(\frac{x^2}{z_x} + \frac{y^2}{z_y} \right). \quad (\text{B.1})$$

The general solution to (2) may be written as a convolution involving the Green's function for the same equation

$$\mathcal{E}(x, y, z) = \frac{-i k}{2\pi z} \int \int dx' dy' \mathcal{E}'(x', y', 0) e^{-\frac{i k}{2} [(x-x')^2/z + (y-y')^2/z]} \quad (\text{B.2})$$

Let us write

$$\mathcal{E}'(x', y', 0) = \mathcal{E}'(x', y', 0) e^{i \frac{k}{2} [x'^2/z_x + y'^2/z_y]}. \quad (\text{B.3})$$

Substitution of expression (B.3) into (B.2) yields

$$\begin{aligned} \mathcal{E}(x, y, z) &= \frac{-i k}{2\pi (z_1 z_2)^{\frac{1}{2}}} \left[\frac{(z_1 z_2)^{\frac{1}{2}}}{z} \right] e^{i \frac{k}{2} \left(\frac{x^2}{z_x - z} + \frac{y^2}{z_y - z} \right)} \\ &\cdot \int \int dx' dy' \mathcal{E}'(x', y', 0) e^{-\frac{i k}{2} \left[\left(\frac{z_1}{z} x - x' \right)^2/z_1 + \left(\frac{z_2}{z} y - y' \right)^2/z_2 \right]} \end{aligned} \quad (\text{B.4})$$

where

$$z_1 = \frac{z}{1 - (z/z_x)} \quad (\text{B.5})$$

$$z_2 = \frac{z}{1 - (z/z_y)}. \quad (\text{B.6})$$

Appendix C

Solution for Fourier Transform of Linearized Hydrodynamic Equations

For convenience we repeat here the general linearized hydrodynamic equations

$$\frac{d\varrho_1}{dt} + \varrho_0 \nabla \cdot \mathbf{v}_1 = 0 \quad (\text{C.1})$$

$$\varrho_0 \frac{d\mathbf{v}_1}{dt} + \nabla p_1 = 0 \quad (\text{C.2})$$

$$\frac{d}{dt} (p_1 - c_s^2 \varrho_1) = (\gamma - 1) \alpha I = S. \quad (\text{C.3})$$

By taking the divergence of (C.2) and introducing

$$\psi = \varrho_0 \nabla \cdot \mathbf{v}_1 \quad (\text{C.4})$$

Equations (C.1) to (C.3) can be reduced to

$$\frac{d\varrho_1}{dt} + \psi = 0 \quad (\text{C.5})$$

$$\frac{d\psi}{dt} + V^2 p_1 = 0 \quad (\text{C.6})$$

$$\frac{d}{dt} (p_1 - c_s^2 p_1) = S. \quad (\text{C.7})$$

We now assume that the source function $S(x, y, t)$ is piecewise linear in time, so that

$$S(x, y, t) = a_n(x, y)(t - t_n) + b_n(x, y); t^n < t < t^{n+1}, \quad (\text{C.8})$$

where

$$a_n(x, y) = [S(x, y, t^{n+1}) - S(x, y, t^n)]/\Delta t \quad (C.9)$$

$$b_n(x, y) = S(x, y, t^n). \quad (C.10)$$

We denote the spatial transform of a variable by the symbol \sim . For example,

$$\tilde{\varrho}(k_x, k_y, t) = \frac{1}{2\pi} \int_{-\infty}^{\infty} \int_{-\infty}^{\infty} dx dy \varrho(x, y, t) e^{-i(k_x x + k_y y)}, \quad (C.11)$$

and we represent $\tilde{\varrho}(k_x, k_y, t^n)$ by

$$\tilde{\varrho}^n(k_x, k_y) = \tilde{\varrho}(k_x, k_y, t^n). \quad (C.12)$$

Transforming (C.5)–(C.7) yields

$$\frac{\partial \tilde{\varrho}_1}{\partial t} - ik_x v \tilde{\varrho}_1 + \tilde{\psi} = 0 \quad (C.13)$$

$$\frac{\partial \tilde{\psi}}{\partial t} - ik_x v \tilde{\psi} - (k_x^2 + k_y^2) \tilde{p}_1 = 0 \quad (C.14)$$

$$\left(\frac{\partial}{\partial t} - ik_x v \right) (\tilde{p}_1 - c_s^2 \tilde{\varrho}_1) = \tilde{a}_n(t - t_n) + \tilde{b}_n. \quad (C.15)$$

Equations (C.13)–(C.15) can be solved by the Laplace transform method, but first it is convenient to introduce the variable change

$$\tilde{\phi}_{\pm}(k_x, k_y, t) \equiv \pm \frac{\tilde{p}_1}{c_s^2}(k_x, k_y, t) + \frac{\tilde{\psi}(k_x, k_y, t)}{ic_s(k_x^2 + k_y^2)^{\frac{1}{2}}}. \quad (C.16)$$

Then

$$\begin{aligned} \tilde{\phi}_{\pm}^{n+1} &= \tilde{\phi}_{\pm}^n \exp\{-i[vk_x \pm c_s(k_x^2 + k_y^2)^{\frac{1}{2}}] \Delta t\} \\ &\pm \frac{1}{c_s^2} \left\{ \left[\frac{\tilde{a}_n}{vk_x \pm c_s(k_x^2 + k_y^2)^{\frac{1}{2}}} - i\tilde{b}_n \right] \right. \\ &\left. + \frac{1 - \exp\{-i[vk_x \pm c_s(k_x^2 + k_y^2)^{\frac{1}{2}}] \Delta t\}}{vk_x \pm c_s(k_x^2 + k_y^2)^{\frac{1}{2}}} \right\} \\ &- \left[\frac{i\tilde{a}_n \Delta t}{vk_x \pm c_s(k_x^2 + k_y^2)^{\frac{1}{2}}} \right] \end{aligned} \quad (C.17)$$

$$\begin{aligned} \tilde{\varrho}_1^{n+1} &= \left[\tilde{\varrho}_1^n - \frac{1}{2}(\tilde{\phi}_+^n - \tilde{\phi}_-^n) \right] \exp(-iv\Delta t k_x) + \frac{1}{2}(\tilde{\phi}_+^{n+1} - \tilde{\phi}_-^{n+1}) \\ &- \frac{\tilde{a}_n}{c_s^2} \left[\frac{1 - \exp(-ivk_x \Delta t)}{v^2 k_x^2} - \frac{i\Delta t}{vk_x} \right] \\ &- \frac{\tilde{b}_n}{c_s^2} \left[\frac{1 - \exp(-ivk_x \Delta t)}{ivk_x} \right]. \end{aligned} \quad (C.18)$$

The solution for $\tilde{\varrho}_1$ can thus be updated by means of (C.17) and (C.18) for the various times $t=0, t^1, \dots, t^n$ and ϱ_1 can be calculated from $\tilde{\varrho}_1$ by means of the DFT. The use of the DFT, of course, imposes periodic boundary conditions on the solution. Before any updating of the solution is possible we must add a buffer region extending at least a distance L in both the x and y -directions. The infinite medium and periodic medium solutions will thus agree for a maximum time $t=L/(c_s + v)$ before periodic “wrap around” affects become apparent.

It is of interest to eliminate ϕ_+ and ϕ_- from (C.18) in order to exhibit the terms which depend on \tilde{a}_n and \tilde{b}_n , since these terms determine the density changes induced by a triangular and a square pulse respectively. We thus obtain

$$\begin{aligned} \tilde{\varrho}_1(k_x, k_y, t) &= -\frac{\hat{a}(k_x, k_y)}{c_s^2} \left\{ [1 - \exp(-ivk_x t)]/(v^2 k_x^2) - it/(vk_x) \right. \\ &\left. - \frac{1}{2} \left[\frac{(1 - \exp\{-i[vk_x + c_s(k_x^2 + k_y^2)^{\frac{1}{2}}] t\})}{[vk_x + c_s(k_x^2 + k_y^2)^{\frac{1}{2}}]^2} - \frac{it}{vk_x + c_s(k_x^2 + k_y^2)^{\frac{1}{2}}} \right] \right\} \\ &- \frac{1}{2} \left[\frac{(1 - \exp\{-i[vk_x - c_s(k_x^2 + k_y^2)^{\frac{1}{2}}] t\})}{[vk_x - c_s(k_x^2 + k_y^2)^{\frac{1}{2}}]^2} - \frac{it}{vk_x - c_s(k_x^2 + k_y^2)^{\frac{1}{2}}} \right] \\ &- \frac{\hat{b}(k_x, k_y)}{c_s^2} \left\{ \left[[1 - \exp(-ivk_x t)]/(ivk_x) \right] \right. \\ &\left. - \frac{1}{2i} \left[\frac{1 - \exp\{-i[vk_x + c_s(k_x^2 + k_y^2)^{\frac{1}{2}}] t\}}{vk_x + c_s(k_x^2 + k_y^2)^{\frac{1}{2}}} \right] \right. \\ &\left. - \frac{1}{2i} \left[\frac{1 - \exp\{-i[vk_x - c_s(k_x^2 + k_y^2)^{\frac{1}{2}}] t\}}{vk_x - c_s(k_x^2 + k_y^2)^{\frac{1}{2}}} \right] \right\}. \end{aligned} \quad (C.19)$$

Appendix D

Method of Calculating Intensity Averages

In assessing the extent of thermal blooming, it is useful to calculate an intensity averaged over some specified area. Unfortunately the choice of a meaningful area is by no means unique. In the Four-D code this problem is solved in the following manner. A number of test intensities are defined as fractions of the peak intensity

$$I_i = f_i I_{\max}. \quad (D.1)$$

Then the number of mesh points N_i are counted for which $I \geq I_i$. This defines an area

$$A_i = N_i \Delta x \Delta y \quad (D.2)$$

over which the intensity obeys $I > I_i$. An average is then calculated of the intensity at those points which make up A_i

$$\bar{I}_i = \frac{1}{N_i} \sum_{k \in A_i} I_k. \quad (D.3)$$

For each A_i there is associated a power

$$P_i(A_i) = A_i \bar{I}_i. \quad (D.4)$$

By linear interpolation on the A_i one can find a value $A_{1/2}$ such that

$$P(A_{1/2}) = P/2, \quad (D.5)$$

where P is the total beam power. The intensity averaged over this area will be

$$\bar{I}_{1/2} = \frac{P}{2A_{1/2}} \quad (D.6)$$

There are many areas which contain one-half the beam power, but clearly the $A_{1/2}$ defined by (D.1)–(D.4) is the minimum half-power area, and it is this feature that makes $A_{1/2}$ unique. The intensity $\bar{I}_{1/2}$ is thus the mean intensity over the minimum half-power area.